Search for right-handed currents in muon decay

A. Jodidio,* B. Balke, J. Carr,† G. Gidal, K. A. Shinsky,‡ H. M. Steiner,
D. P. Stoker,§ M. Strovink, and R. D. Tripp
Lawrence Berkeley Laboratory and Department of Physics, University of California, Berkeley, California 94720

B. Gobbi
Department of Physics, Northwestern University, Evanston, Illinois 60201

C. J. Oram
TRIUMF, Vancouver, British Columbia V6T 2A3, Canada
(Received 27 May 1986)

Limits are reported on charged right-handed currents, based on precise measurement of the end-point e^+ spectrum in μ^+ decay. Highly polarized μ^+ from a TRIUMF "surface" muon beam were stopped in pure metal foil and liquid-He targets selected to minimize depolarization effects. In the stopping target region either a spin-precessing transverse field (70 or 110 G) or a spin-holding longitudinal field (0.3 or 1.1 T) was applied. Data collected with the spin-precessing field were used for the momentum calibration of the spectrometer. The spin-held data were used to measure the relative e^+ rate at the momentum end point in a direction opposite to the μ^+ spin. In terms of the standard muon-decay parameters this rate is given by $(1-\xi P_\mu \delta/\rho)$ where P_μ is the muon polarization. The combined 90% confidence lower limit from the analysis presented in this paper and our earlier analysis of the spin-precessed data by means of the muon-spin-rotation (μSR) technique is $\xi P_\mu \delta/\rho > 0.9975$. For models with manifest left-right symmetry and massless neutrinos this result implies the 90% confidence limits $m(W_2) > 432$ GeV/c^2 and $-0.050 < \zeta < 0.035$, where W_2 is the predominantly right-handed boson and ζ is the left-right mixing angle. Limits are also deduced on the $\nu_{\mu L}$ mass and helicity in π^+ decay, non-$(V-A)$ couplings in helicity projection form, the mass scale of composite leptons, and the branching ratio for $\mu \to e + f$ where f (familon) is the neutral massless Nambu-Goldstone boson associated with flavor-symmetry breaking.

I. INTRODUCTION

In the widely accepted Glashow-Weinberg-Salam (GWS) $SU(2)_L \times U(1)$ model of weak and electromagnetic interactions[1] the $V-A$ structure of weak interaction has been put in *a priori* to obtain agreement with experiments. Although the model agrees with all experimental results up to presently available energies, experimental precision has not been sufficient to rule out relatively large deviations from the $V-A$ structure.[2] We have made a sensitive search for such deviations by measuring the muon-decay spectrum near the end point. Our result is particularly suited for setting stringent limits on charged right-handed, i.e., $V+A$, currents, and for constraining parameters in the left-right-symmetric models.

The left-right-symmetric (LRS) models,[3] based on the gauge group $SU(2)_R \times SU(2)_L \times U(1)$, have been studied intensively as extensions of the standard GWS model. In such models L-R symmetry is broken spontaneously at moderate energies, with the predominantly right-handed gauge boson W_2 acquiring a heavier mass than the predominantly left-handed W_1 (Ref. 4). This accounts for the left-handed couplings observed to be dominant at low energies, while restoring parity conservation at higher energy. The mass-squared ratio of physical bosons W_1 and W_2 will be denoted by

$$\epsilon = m^2(W_1)/m^2(W_2) .$$

The mass eigenstates W_1 and W_2 are related to W_L and W_R by a mixing angle ζ:

$$W_1 = W_L \cos\zeta - W_R \sin\zeta ,$$

$$W_2 = W_L \sin\zeta + W_R \cos\zeta .$$

Limits on charged right-handed currents that can be obtained from leptonic and semileptonic weak processes depend on the masses of the associated right-handed neutrinos. If neutrinos are Dirac fermions, ν_L and ν_R must necessarily have the same mass, since they are different helicity states of the same particle. In this case the predominantly right-handed boson W_2 participates in low-energy processes. However, in some attractive models neutrinos are Majorana particles.[5] Since there can be both Majorana and Dirac mass terms in the neutrino mass matrix, the physical neutrinos ν_1 and ν_2 may have different masses. In most models the predominantly left-handed neutrino ν_1 is predicted to be very light, $m(\nu_{l1}) \sim m_l^2/m(W_2)$, while the predominantly right-handed neutrino ν_2 is very heavy, $m(\nu_2) \sim m(W_2)$, and therefore cannot be produced in low-energy experiments. The physical neutrinos ν_1 and ν_2 are related to ν_L and ν_R by a mixing angle δ, expected to be of the order of $m_l/m(W_2)$. Ignoring the very small neutrino mixing angle, purely leptonic processes, requiring production of at least one ν_2, do not set limits on right-handed currents in such theories. Semileptonic processes such as νN and $\bar{\nu} N$ scattering,

which do not require production of ν_2, can still set a limit on the mixing angle ζ.

Hadronic weak processes set limits on right-handed currents independently of ν_R masses. In a class of models, called "manifestly" L-R symmetric, the left-handed and right-handed Kobayashi-Maskawa quark mixing angles are assumed to be identical, and CP invariance is assumed to hold. In these models the K_L-K_S mass difference requires $m(W_2) > 1.6$ TeV (Ref. 6), and current-algebra analysis of $\Delta S = 1$ decays yields $\zeta \leq 0.004$, $m(W_2) > 300$ GeV for $\zeta = 0$ (Ref. 7). If left-handed and right-handed mixing angles are not identical hadronic processes are consistent with $m(W_2) \geq 300$ GeV (Ref. 8). Another strong limit $\zeta < 0.005$ has been obtained in a model-dependent analysis of semileptonic weak processes, again assuming manifest L-R symmetry.[9]

Figure 1 exhibits contours corresponding to 90% confidence limits[10] on ϵ and ζ from experiments in β decay, μ decay, and $\nu N, \bar{\nu} N$ scattering. The allowed regions contain the origin $\epsilon = \zeta = 0$, which is the $V-A$ limit. Manifest L-R symmetry has been assumed. The contours from μ- and β-decay experiments have been plotted with the assumption that the right-handed neutrinos are sufficiently light not to affect the kinematics. The bold ellipse in Fig. 1 is the combined result from the analysis of the muon-decay spectrum end point opposite the μ^+ spin, presented in this paper, and from our μSR analysis.[11,12] The other muon-decay contours are derived from the measurement[13] of the polarization parameter ξP_μ (dotted curve) and the Michel parameter[14] ρ (solid curve). Nuclear β-decay contours are derived from the Gamow-Teller β polarization[15] (dot-dashed curve); the comparison of Gamow-Teller and Fermi β polarizations[16] (long-dashed curves); and the ^{19}Ne asymmetry $A(0)$ and ft ratio,[17] with the assumption of conserved vector current (short-dashed curves). The limits from the y distributions[18] in $\nu N, \bar{\nu} N$ scattering (double lines) are valid irrespective of ν_R mass.

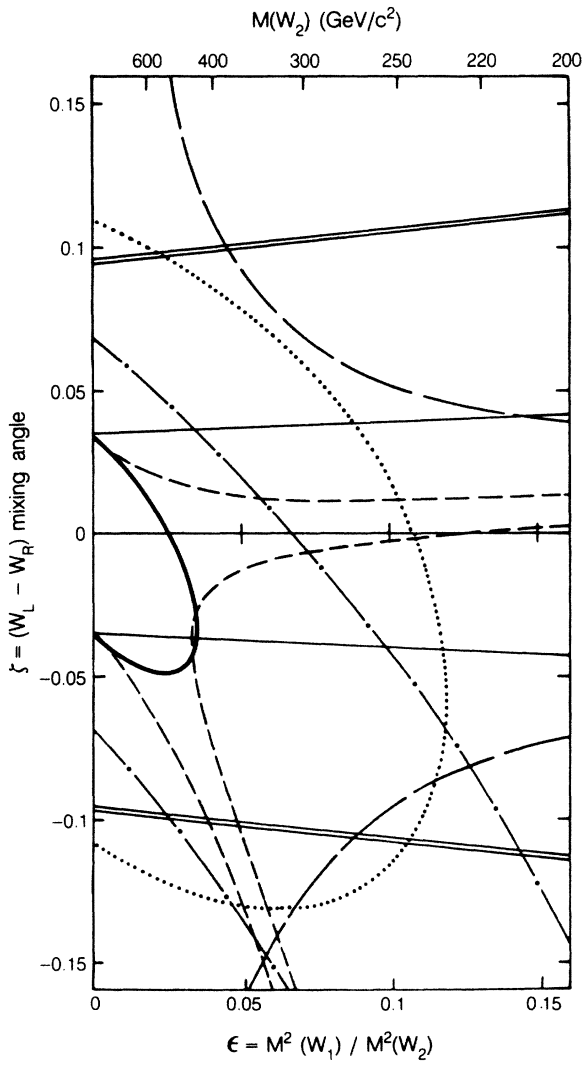

FIG. 1. Experimental 90% confidence limits on the mass-squared ratio ϵ and mixing angle ζ for the gauge bosons W_1 and W_2. The allowed regions are those which include $\epsilon = \zeta = 0$. The bold ellipse is the combined result from the analysis presented in this paper and from our μSR analysis (Refs. 11 and 12). The sources of the other limits are described in the text.

Section II of this paper discusses the properties of the muon-decay spectrum and their application to the data analysis. The beamline and experimental apparatus are discussed in Sec. III. Event reconstruction and selection are considered in Sec. IV. Data analysis and data fitting results are presented in Sec. V, and systematic errors are discussed in Sec. VI. The conclusions from the experimental result are drawn in Sec. VII.

II. MUON-DECAY SPECTRUM

The muon differential decay rate for an interaction mediated by a heavy vector boson W differs from the decay rate computed with the corresponding four-fermion contact interaction Hamiltonian by terms[19] of order $(m_\mu/M_W)^2$. These terms are $\approx 10^{-6}$ for $M_W \approx 80$ GeV/c^2 and are negligible at the present level of experimental precision. Consequently we will use the expression for the muon-decay spectrum computed for a four-fermion contact interaction. We will also assume that neutrinos are sufficiently light not to affect the kinematics. We will return to the question of massive neutrinos in Sec. VII G.

Without radiative corrections, the muon differential decay rate,[20] integrated over e^+ spin directions, is given by

$$\frac{d^2\Gamma}{x^2 dx\, d(\cos\theta)} \approx \left[(3-2x) + (\tfrac{4}{3}\rho - 1)(4x-3) + 12\frac{m_e}{m_\mu}\frac{x-1}{x}\eta \right] - [(2x-1) + (\tfrac{4}{3}\delta - 1)(4x-3)]\xi P_\mu \cos\theta \,. \tag{2.1}$$

Here x is the reduced energy $E_e/E_{\max}$, where $E_{\max} = (m_e^2 + m_\mu^2)/(2m_\mu) = 52.83$ MeV is the maximum energy and m_e and m_μ are the particle masses. The effects of finite positron mass are neglected in the above formula but not in the analysis. The angle between the positron momentum and the muon polarization vector

TABLE I. Values of the muon-decay parameters ρ, η, ξ, and δ in the $V-A$ model and in the manifestly left-right-symmetric (LRS) model with massless neutrinos. Their world-average experimental values (Ref. 21) prior to our experiment are also listed. The values in the LRS model are given to the lowest order in the mass-squared ratio ϵ and mixing angle ζ for the gauge bosons W_1 and W_2.

Decay parameter	$V-A$ value	Value in the LRS model	Experimental value
ρ	$\frac{3}{4}$	$\frac{3}{4}(1-2\zeta^2)$	0.7517 ± 0.0026
η	0	0	$0.06\ \pm0.15$
ξ	1	$1-2\epsilon^2-2\zeta^2$	ξP_μ: $0.972\ \pm0.014$
P_μ[a]	1	$1-2(\epsilon+\zeta)^2$	
δ	$\frac{3}{4}$	$\frac{3}{4}$	0.7551 ± 0.0085

[a] P_μ is the muon longitudinal polarization from π^+ decay at rest.

P_μ in the μ^+ rest frame is $\pi-\theta$. The world-average values[21] of the muon-decay parameters ρ, η, ξ, and δ measured prior to our experiment are given in Table I. Also given there are their values in the L-R-symmetric model, to lowest order in ϵ and ζ. The $V-A$ values correspond to $\epsilon=\zeta=0$.

The first-order electromagnetic corrections to the muon-decay spectrum are of order $\alpha\ln(m_\mu^2/m_e^2)$ (several %). They can be computed accurately with the four-fermion contact interaction Hamiltonian,[22] since the heavy intermediate vector bosons contribute negligible additional terms[23] of order $\alpha(m_\mu/m_W)^2$. The first-order corrections have been computed for the general Fermi interaction,[24] and this general expression was used in Monte Carlo simulations to verify the accuracy of the analysis method. For the analysis itself only the $V-A$ corrections were needed.

The radiatively corrected muon-decay spectrum for a pure $V-A$ interaction is shown in Fig. 2 for $\cos\theta$ equal to -1, 0, and $+1$. The spectrum for unpolarized muons corresponds to the $\cos\theta=0$ curve, whose sharp edge at $x=1$ played an important role in the spectrometer momentum calibration. For $\cos\theta=1$, angular-momentum conservation forces the $V-A$ rate to vanish. The $V+A$ spectrum at $\cos\theta$ is equivalent to the $V-A$ spectrum at $(-\cos\theta)$. The region of greatest experimental sensitivity to an admixture of right-handed currents is therefore near $x=1$ and $\cos\theta=1$, where the $V-A$ rate vanishes while the $V+A$ rate is maximum. The experiment was designed to measure the positron spectrum for $x>0.85$ and $\cos\theta>0.95$.

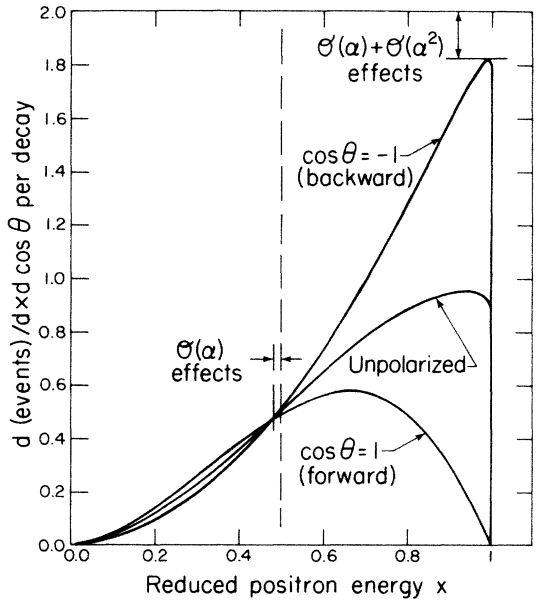

FIG. 2. The $V-A$ radiatively corrected muon-decay spectrum plotted for $\cos\theta=+1$, 0, and -1, where $\pi-\theta$ is the angle between the positron direction and the muon spin. The effects of radiative corrections are also indicated.

The data analysis was based on a simple property of the muon-decay spectrum: if the weak interaction is predominantly $V-A$, with a small admixture of $V+A$, scalar, tensor, or pseudoscalar currents, then the positron spectrum near the end point, for $\cos\theta\approx1$, can be expressed as a sum of the $P_\mu\cos\theta=1$ $V-A$ spectrum, which vanishes linearly at $x=1$, and the $P_\mu\cos\theta=0$ $V-A$ spectrum, which is flat near $x=1$ with a step to zero at the end point. The relative size of the step at the end point is $1-\xi P_\mu\cos\theta\,\delta/\rho$. Measurement of the rate as a function of $\cos\theta$ allows us to extract $\xi P_\mu\delta/\rho$.

We introduce

$$\tilde{\rho}=1-\tfrac{4}{3}\rho\ ,$$

$$\tilde{\delta}=1-\tfrac{4}{3}\delta\ ,$$

with $\tilde{\rho}=\tilde{\delta}=0$ for a pure $V-A$ interaction, and the decay spectra: $S(x,P_\mu\cos\theta)$ is the spectrum for an arbitrary weak coupling (i.e., arbitrary values of ξ,ρ,δ); $S_{V-A}(x,1)$ is the $V-A$ spectrum at $P_\mu\cos\theta=1$, $S_{V-A}(x,0)$ is the $V-A$ spectrum at $P_\mu\cos\theta=0$. The latter two spectra are normalized to $S(x,P_\mu\cos\theta)$. Ignoring the η term in (2.1), which is negligible near the end point, and ignoring radiative corrections, we can write

$$S(x,P_\mu\cos\theta)=q(\theta)S_{V-A}(x,1)+r(\theta)S_{V-A}(x,0)\ , \qquad (2.2)$$

where

$$q(\theta)=\xi P_\mu\cos\theta-\tfrac{1}{2}\tilde{\delta}\xi P_\mu\cos\theta+\tfrac{1}{2}\tilde{\rho}\ , \qquad (2.3)$$

and $r(\theta)$ is the relative rate at the end point:

$$r(\theta)=(1-\xi P_\mu\cos\theta)+\tilde{\delta}\xi P_\mu\cos\theta-\tilde{\rho}\ . \qquad (2.4)$$

To lowest order in $\tilde{\rho}$, $\tilde{\delta}$, and $(1-P_\mu\cos\theta)$, $r(\theta)$ and $q(\theta)$ take the simpler forms

$$r(\theta)=1-\xi P_\mu \frac{\delta}{\rho}\cos\theta \tag{2.5}$$

and

$$q(\theta)=1-r(\theta)=\xi P_\mu \frac{\delta}{\rho}\cos\theta\ . \tag{2.6}$$

When radiative corrections are included, the exact relation (2.2) becomes only an approximation, as does (2.5). For the fitting procedure to be described in Sec. V A, and for a spectrum given by a combination of only $V+A$ and $V-A$ effective couplings, the radiative corrections were found to have only a negligible effect on $r(\theta)$. When this experiment is used for setting limits on the presence of other effective weak couplings, one expects that, when all couplings are taken into account, the radiative corrections likewise do not introduce a significant additional systematic error. Calculations to check this expectation must be made specifically for the particular combination of couplings being investigated, and so are not included here.

The highly polarized muons in our experiment were supplied by a "surface" muon beam,[25] derived from pions decaying at rest near the surface of the production target. Right-handed currents would reduce the muon polarization in pion decay to $P_\mu=1-2(\epsilon+\zeta)^2$ (assuming manifest left-right symmetry). Including this effect, our final result is given to lowest order in ϵ and ζ by

$$\xi P_\mu \frac{\delta}{\rho}=1-2(2\epsilon^2+2\epsilon\zeta+\zeta^2)\ . \tag{2.7}$$

Since we are unable to correct for all possible sources of muon depolarization, our result should be interpreted as a lower limit on $\xi P_\mu \delta/\rho$.

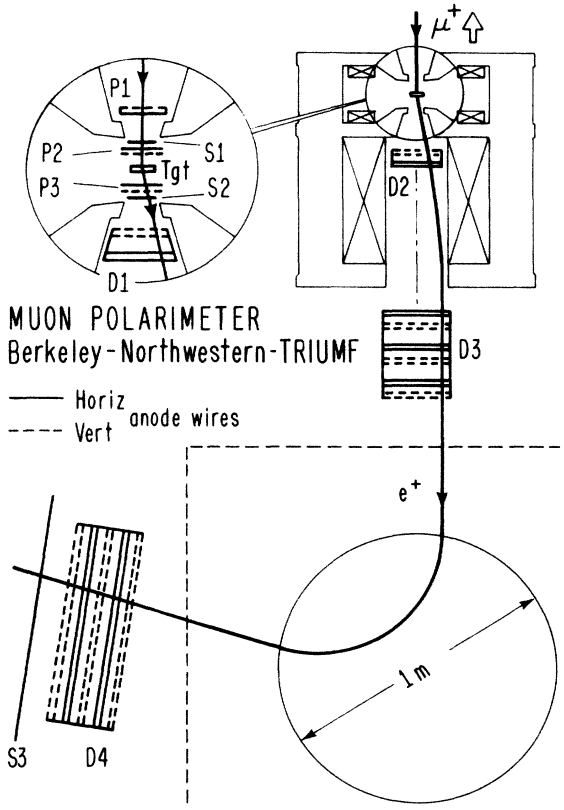

FIG. 3. Plan view of muon polarimeter. P1—P3 are proportional chambers; S1—S3 are scintillators; D1—D4 are drift chambers. The veto scintillators V1 and V2 surrounding S1 and S2, respectively, are not shown. Muons entering the solenoid are stopped in the target. Decay e^+ emitted near the beam direction are focused by the solenoid into the spectrometer.

III. EXPERIMENTAL METHOD

A. Overview

The experiment was performed in the M13 beamline of the TRIUMF cyclotron. Surface muons were transported in vacuum to a stopping target in the muon polarimeter, shown in Fig. 3. High-purity metal foils (Ag, Al, Au, Cu) and liquid He were selected as stopping targets, since in these materials muonium (μ^+-e^- atom) formation, leading to muon depolarization, is strongly suppressed.

The target region was immersed either in a strong longitudinal "spin-holding" field (0.3 or 1.1 T) aligned opposite to the nominal beam direction, or a vertical (70 or 110 G) spin-precessing field. The longitudinal field quenched the muon depolarization in muonium via the Paschen-Back effect. The data collected with the longitudinal field were used to measure the rate at the spectrum end point, and data with the spin-precessing field were used in the momentum calibration of the spectrometer.

The angular acceptance for positrons was significantly increased by the downstream portion of the solenoid, which served as a solenoidal field lens, focusing the positrons into the dipole magnet spectrometer. The septum between the target and solenoid bore made the focal length of the solenoid lens nearly independent of the choice of target field orientation.

A horizontally focusing spectrometer was chosen in order to achieve a high momentum resolution. The windows of the vacuum box between the magnet poles were positioned close to the focal planes to minimize the effects of Coulomb scattering on momentum resolution.

Particle trajectories in the target region (see Fig. 3 inset) were measured by the proportional chambers P1 and P2 for muons, and by the proportional chamber P3 and drift chambers D1 and D2 for positrons. Near the spectrometer magnet, drift chambers D3 and D4 measured positron tracks. Scintillation counters S1, S2, and S3 provided trigger signals.

The data were accumulated in three running periods over 3 years at TRIUMF. The experimental conditions were essentially the same for all three runs, except for minor differences mentioned below and in Appendix A. The longitudinal field in the stopping target region was 1.1 T for runs 1 and 2, and 0.3 and 1.1 T for run 3. A total of 1.8×10^7 (1.4×10^7) triggers were collected in the spin-holding (spin-precessing) mode on 130 (170) computer tapes [1600 BPI (bytes per inch)]. Under optimal conditions these data could have been accumulated in ~20 d of continuous running. In each of the periods data were also collected in many special runs, to be described in Sec. IV, which were used to calibrate the spectrometer.

The muon beam, muon polarimeter, and trigger will now be described in greater detail. We will also briefly review the process of muon deceleration to thermal energies and the suppression of muon depolarization in muonium by the longitudinal field.

B. The beamline

The M13 beamline[26] at the TRIUMF meson facility is a low-energy (20—130 MeV/c) muon and pion channel, which views a 2- or 10-mm-thick carbon production target at 135° with respect to the primary proton beam (Fig. 4). The particles are transported in vacuum through two 60°-bending dipoles, with momentum-selecting slits at the two foci allowing a momentum bite $\Delta p/p$ as low as 0.5%. At a typical proton beam current of 100 μA, the beamline was tuned to deliver about 15000 μ^+ per sec in a 1% momentum interval, focused in a 0.3-msr cone on a ~1-cm-radius spot at the muon-stopping target.

Positive-particle fluxes[26] in the beamline are shown in Fig. 5. Below 29.8 MeV/c the muon flux is dominated by muons produced by pions decaying at rest near the surface of the production target. At our beamline setting of 29.5 MeV/c these surface muons constituted over 98% of the muon flux. In the absence of right-handed currents and

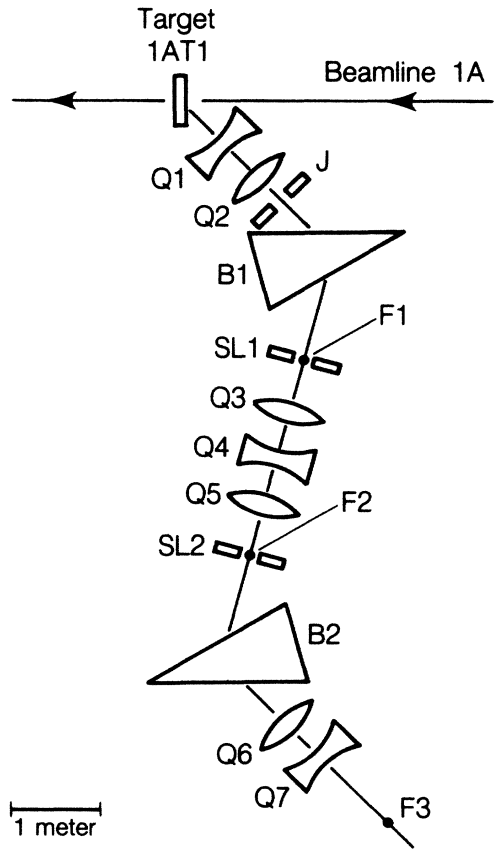

FIG. 4. The M13 beamline at TRIUMF. B1 and B2 are dipoles; Q1—Q7 are quadrupoles; F1—F3 are foci; the slits SL1 and SL2 and the jaws J have adjustable horizontal and vertical apertures.

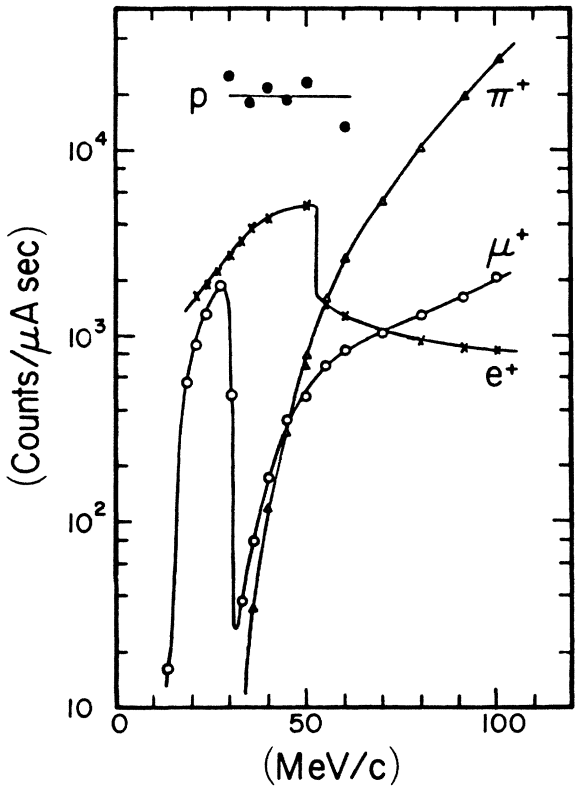

FIG. 5. Positive particle fluxes vs beamline momentum settings in the M13 beamline at TRIUMF (taken from Ref. 26). The data were collected with all slits and jaws in the beamline fully open.

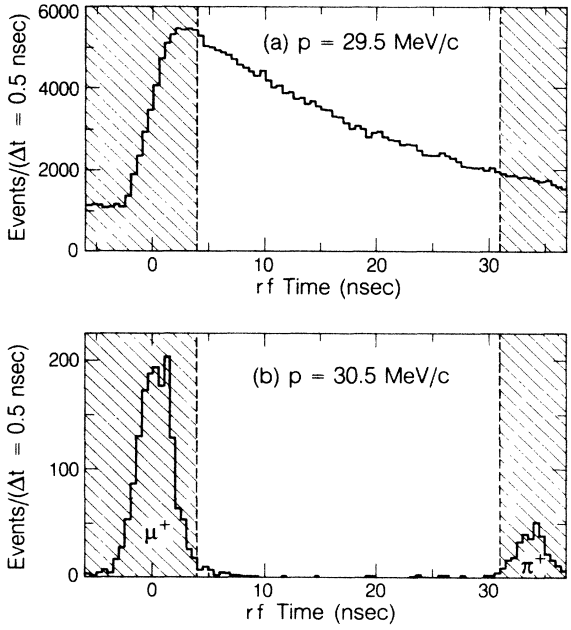

FIG. 6. Beam particle arrival times at the stopping target with respect to the cyclotron rf cycle at (a) 29.5 MeV/c and (b) 30.5 MeV/c. The shaded regions, containing almost all of the cloud μ^+ and prompt π^+ contaminations, were rejected.

scattering they were expected to be fully polarized. The remaining 1.5% of the muon flux consisted of "cloud" muons produced by pions decaying in flight. The cloud muons were not highly polarized, and were removed from the event sample.

The time structure of the TRIUMF proton beam consisted of 2–5 nsec bursts every 43 nsec. The cloud muons had to be produced in close proximity to the production target, i.e., within a few nsec of the bursts, in order to be transported by the beamline. Thus, they could be eliminated by a cut on arrival time at the stopping target, measured with respect to the cyclotron rf signal.

The arrival time distribution is shown in Fig. 6 for beamline settings of 29.5 MeV/c (normal) and 30.5 MeV/c (cloud muons enhanced). At 29.5 MeV/c [Fig. 6(a)] the arrival rate is dominated by the surface muons, which exhibit an exponential time distribution corresponding to the pion lifetime. At 30.5 MeV/c [Fig. 6(b)], two isolated peaks corresponding to the cloud muons and to pions are evident. These were eliminated by the timing cut shown by the shaded regions. Other particles in the beamline were protons, which stopped in the beamline vacuum window, and positrons, which passed through the stopping targets and were rejected by the trigger requirement.

C. Muon deceleration and thermalization

First we briefly review the suppression of muon depolarization in muonium by the longitudinal magnetic field. Using the magnetic field direction as the spin-quantization axis, we express the muonium energy eigenstates in terms of $y = |B|/(1585\ \text{G})$ in a "natural" basis $|m_\mu m_e\rangle$:

$$|++\rangle ,$$
$$s|+-\rangle + c|-+\rangle ,$$
$$c|+-\rangle - s|-+\rangle ,$$
$$|--\rangle ,$$

where $|+-\rangle$ means $|m_\mu = +\frac{1}{2}, m_e = -\frac{1}{2}\rangle$, etc., and

$$c = (1/\sqrt{2})[1 + y(1+y^2)^{-1/2}]^{1/2} ,$$
$$s = (1/\sqrt{2})[1 - y(1+y^2)^{-1/2}]^{1/2} .$$

For simplicity, suppose that all muons arrive with a spin parallel to the field. Then half of the muonium ensemble is formed in the state $|++\rangle$ and half in the state $|+-\rangle$. The state $|++\rangle$ is stationary, so the muon polarization of half of the ensemble is preserved. The polarization for the other half of the ensemble oscillates between

$$P_\mu = (c^2 - s^2)^2 - 4s^2c^2 = (y^2-1)(y^2+1)^{-1}$$

and $P_\mu = 1$ with an angular frequency of $2.3(1+y^2)^{1/2}$ GHz. The net polarization is thus $P_\mu = \frac{1}{2}(2y^2+1)(y^2+1)^{-1}$, different from unity by the quantity $\frac{1}{2}(y^2+1)^{-1}$, which is small when the field is large.

Muons reached the stopping target with a kinetic energy of ~ 3.3 MeV, after traversing 50 mg/cm^2 of material (mostly windows, wires, and gas) upstream of the target. As the μ^+ slows down to thermal velocities, the main energy-loss processes depend on its kinetic energy.[27] Above 2–3 keV the energy loss is due to scattering with (unpolarized) electrons, which partially depolarize the μ^+ through spin exchange.[28] The correction due to such depolarization is evaluated in Appendix E. At 2–3 keV the μ^+ velocity is comparable to that of the valence electrons of the medium, and muons begin to capture and lose electrons rapidly, forming a succession of short-lived muonium states. Again, energy is lost in collisions with electrons. Below 200 eV the energy loss is due to collisions of a stable muonium atom with atoms and molecules. The time spent by the decelerating μ^+ in muonium states ($\sim 10^{-12}$ sec) is too short for the hyperfine transitions to cause appreciable depolarization.[29]

The state in which the μ^+ is finally thermalized depends on the medium. In many nonmetals muons are thermalized as muonium. In metals, however, the μ^+ are thermalized in a quasifree state, because the high-conduction electron concentration effectively screens the μ^+ from interactions with individual electrons. For this reason most of our data was collected with high-purity ($\geq 99.99\%$) metal foils (Ag, Al, Au, Cu) as stopping targets (Appendix A). The remainder was collected with liquid He, where muonium is disfavored in the final state due to the large difference between the ionization potential of He (24.6 eV) and muonium (13.5 eV). The energetically favored final state in liquid He (in which the μ^+ polarization is expected to be preserved) is the molecular ion $He\mu^+$ with binding energies of 1.9 eV for the ground state and 1.2 eV for the first vibrational state. However, we found in our experiment that liquid He is 12% depolarizing without the strong longitudinal field.[12] A possible explanation is that if muons are thermalized as muonium, they survive in this form for a considerable time because of the improbability of encountering a He^+ ion with which to combine into $He\mu^+$.

Although the strong longitudinal field is sufficient to quench μ^+ depolarization in muonium, it cannot "hold" the spins of quasifree muons in metal targets. The energy difference between states in which the muon spin is parallel or antiparallel to the 1.1 T (0.3 T) field is only 6.2×10^{-7} eV (1.7×10^{-7} eV), while the room-temperature thermal energy is $kT = 2.6\times10^{-2}$ eV. Relaxation of the muon spins toward the equilibrium situation, where the number of spins parallel or antiparallel to the applied field are almost equal, requires the presence of oscillating magnetic fields with angular frequency 9.4×10^8 sec^{-1} for a 1.1-T longitudinal field (2.6×10^8 sec^{-1} at 0.3 T). Such fields may be provided by the nuclear magnetic dipole moments. The stopped muon polarization would then decay exponentially towards thermal equilibrium with a characteristic spin-lattice relaxation time T_1. Section V C compares the results for $\xi P_\mu \delta/\rho$ from different decay time intervals in order to test for possible spin relaxation.

D. The muon polarimeter

The muon polarimeter is shown schematically in Fig. 3. Muons traversed about 50 mg/cm^2 of material before be-

ing stopped in metal foil or liquid-He targets, placed on the axis between the first two coils of the solenoid magnet. The solenoid magnet served two purposes. The downstream portion, with a bore of 11-cm radius, served as a 0.5-T m field lens, focusing the decay positrons into the dipole magnet spectrometer. The upstream portion produced a 0.3- or 1.1-T longitudinal spin-holding field applied to quench muon depolarization in muonium. The angle between the solenoid's field and its axis was less than arccos (0.999 99) in the fiducial target area.

The experiment was run in two modes, corresponding to two different field orientations in the target region. In the spin-holding mode a strong longitudinal field was applied to suppress muon depolarization, and the spin-held data were used to measure the decay rate at the end point. In the spin-precessing mode a 70- or 110-G vertical field replaced the longitudinal field, nulled to within ± 2 G by means of a small adjustable current applied to the upstream coils. The null condition was indicated by a peak in the ratio of events to stopped μ^+ in run 1, and by field measurements in runs 2 and 3. After appropriate cuts on muon-decay time, the spin-precessed data were effectively unpolarized, and could be used to calibrate the spectrometer.

The primary design goal of the positron spectrometer was to achieve a high momentum resolution while maintaining an acceptance of ≥ 250 msr in combination with the target solenoid. In order to minimize the adverse effects of multiple Coulomb scattering on momentum resolution, a horizontally focusing spectrometer was chosen, which bent the $x = 1$ e^+ trajectories by 98°. The 37-in.-diameter dipole magnet with approximate cylindrical symmetry (originally used by Sagane, Dudziak, and Vedder[30]) provided nearly symmetric point-to-point focusing for particles between the focal planes which were ~ 1 m from the center of the magnet. The intervening volume between the conjugate focal planes was evacuated, with the Mylar vacuum box windows positioned close to the focal planes.

The combined solenoid lens-spectrometer magnet system accepted particles over a $\pm 15\%$ momentum range and decay angles relative to the solenoid axis less than arccos (0.95). In the final analysis we use events only from a subportion of this phase space.

The spectrometer magnet was powered continuously, and the NMR-monitored central field of 0.32 T drifted by less than 1 G over a period of several weeks. To minimize the effect of this and other possible drifts in the spectrometer calibration, the target field was switched approximately hourly between the spin-holding and spin-precessing orientations. Each tape of spin-held data then was either preceded or followed by a tape of calibrating spin-precessed data.

Particle trajectories in the target region (Fig. 3 inset) were measured by proportional chambers P1 and P2 for the incoming muons, and by proportional chamber P3 and drift chambers D1 and D2 for the outgoing positrons. Scintillation counters S1 (0.005 in. thick), just upstream of P1, and S2 (0.010 in. thick), just downstream of P3, provided trigger signals. The thickness of scintillation counter S1 was kept to a minimum to minimize the chance of a muon stopping upstream of the target and to minimize Coulomb scattering. Veto scintillation counters V1 and V2 (0.125 in. thick), just in front of S1 and behind S2, respectively, had 1.5-in.-diameter aperture-defining holes around the solenoid axis. All scintillation counters were viewed from left and right by photomultipliers. Positron track coordinates near the spectrometer focal planes were measured by low-mass drift chambers D3 and D4. Scintillation counter S3 provided trigger signals from positrons exiting the spectrometer.

The proportional chambers and drift chambers were run on a 92% methane-8% methylal gas mixture, selected to minimize Coulomb scattering. Chamber resolutions and efficiencies will be discussed in Sec. IV.

E. The Trigger

The trigger was based on fast signals from the scintillation counters and the cathode planes of the proportional chambers. It required the signature of a particle stopping in the target, followed by a positron in delayed coincidence of 0.1—10 μsec registered by detectors downstream. With detector signals denoted by their symbols in Fig. 3, the trigger requirement was $P1\cdot\overline{V1}\cdot S1\cdot P2\cdot\overline{P3}\cdot\overline{S2}\cdot\overline{V2}$ delayed in coincidence with $P3\cdot S2\cdot S3\cdot\overline{V1}\cdot\overline{V2}$. Placement of S1 upstream of the less massive P2 minimized the probability of a muon stopping in the last detector element required for the muon part of the trigger, and allowed more precise measurement of the transverse coordinates of the stopped muon. The gain of S1 was set to make it efficient for muons, but not for the beam positrons, which deposited 8 times less energy.

Events were tagged if a particle was detected upstream of the stopping target within 0.3—10 μsec after a muon stop. Such events had a high probability for the decay positron to be produced by an extra muon in the target, rather than by the muon causing the trigger. These events were rejected in analysis if the extra particle was detected before the decay positron. As a result of this cut only a very small fraction ($\sim 0.1\%$) of events in the final sample had positrons produced by extra muons. The small fraction that remained was due to extra muons arriving before the muon causing the trigger, or within the 300-nsec notch after the registered muon stop. (This notch was necessary because of afterpulsing in the proportional chambers P1 and P2.) The systematic error due to events with positrons produced by extra muons was found to be negligibly small ($< 1\times 10^{-4}$).

Beam positrons, which constitute $\sim 60\%$ of the M13 beam flux at 29.5 MeV/c, passed through the stopping targets and apparatus and stopped in lead shielding next to the low-momentum side of the vacuum tank in the spectrometer magnet. Since these positrons failed to exhibit the signature of a muon stopping in the target or of a positron reaching trigger counter S3, and since they possessed only 60% of the minimum momentum required for analysis, they did not constitute a background.

IV. EVENT RECONSTRUCTION AND SELECTION

Track reconstruction was relatively simple since there was only one incoming and one outgoing track, and all

wire-chamber planes were better than 90% efficient with little noise. However, reconstruction of curved tracks in the solenoid magnet required a special fit that used a first-order optics approximation for the cylindrically symmetric field there.

Initially all e^+ track segments were fitted with straight lines. Positron track segments were found separately in the horizontal and vertical projections of three groups of wire chamber planes (Fig. 3): P3, D1, D2 (five vertical and five horizontal wire planes), D3 (six and six), and D4 (six and four). All possible hit combinations were considered, and a track with a minimum χ^2 was selected among those that had hits in the maximum number of planes. A combination of hits was considered to be a track if the total χ^2 was below a maximum value corresponding to a hit accuracy of ~ 1 mm in D3 and D4 and ~ 2 mm in P3 through D2.

In 99% of the triggers, tracks were found in all six segments. 13% of the triggers were rejected to avoid ambiguities due to high or low hit multiplicities associated with the μ^+ or e^+ track. To achieve greater accuracy in the $\cos\theta$ measurement, positron tracks were required to have unambiguous hits in both the horizontal and vertical planes of P3, and at least three hits were required in each projection of the e^+ track inside the solenoid. 95% of events in the final sample had the e^+ track portion inside the solenoid recorded by at least nine wire planes.

Muon tracks were accepted if they were unambiguous, or if there were no more than two hits in one and only one of the P2 planes. In the latter case (5% of the final sample) we selected the track which in extrapolation to the stopping target was closest to the decay vertex indicated by the e^+-track extrapolation.

Track segments in the solenoid were then refitted in both projections simultaneously in the first-order optics approximation for cylindrically symmetric fields.[31] In this approximation particle trajectories through the solenoid are determined from initial conditions by means of transfer matrices, computed from magnetic rigidity and field values on the solenoid axis. Curved tracks could therefore be fitted without detailed step-by-step computation of orbits in the magnetic field. Incoming and outgoing tracks were extrapolated to the stopping target, so that the angle θ between the muon and electron tracks could be determined at the decay vertex. It was found from the Monte Carlo simulation, which propagated particles through the full magnetic field in small steps, that the first-order optics approximation determined $\cos\theta$ with excellent accuracy (Sec. VI D).

Careful attention was paid to chamber calibration. All chamber planes were aligned in the transverse direction; the residual means were less than 50μ. In the drift chambers the nonlinear time-distance relationships were obtained separately for each plane of every chamber. In an initial approximation the time-distance relationships were found by integrating the flux versus drift time and assuming uniform cell illumination. They were then dynamically fine-tuned by making small adjustments to minimize track residuals. The procedure converged after 1500 events. Residuals of $\sigma < 500\mu$ were achieved in D1 and D2, with the exception of two planes in D1 where σ was $\approx 700\mu$. Residuals in D3 and D4 had $\sigma < 250\mu$. In the proportional chambers, up to three contiguous wires (spaced at 2 mm) were considered as a single acceptable hit. Events with four or more contiguous wires hit were rejected.

Positron tracks were required to link in the following extrapolations: in radius and azimuth in the solenoid magnet between D2 and D3; in vertical slope and vertical position inside the spectrometer magnet; and in impact parameter with respect to the central axis of the approximately cylindrically symmetric field of the spectrometer. Muon and positron extrapolations to the decay vertex at the stopping target were required to match within 4 mm. Track linkage requirements resulted in a 30% loss of events. Events near the edges of geometrical acceptance were cut to avoid particles that were scattered back into the apparatus (20% event loss). Other small fiducial cuts were made to protect against event ambiguity.

The horizontal focusing property of the spectrometer allowed the e^+ momentum to be reconstructed from the sum of horizontal coordinates at the two conjugate focal planes. This sum was empirically corrected with momentum-dependent first- or second-order terms in three variables: mean vertical deviation from the median plane of the spectrometer, impact parameter with respect to the spectrometer axis, and vertical position at the spectrometer exit. Initially, the corrections were obtained from special calibration runs in which the beamline momentum bite was reduced to 0.5% $\Delta p/p$, and beam positrons, in 3% to 5% steps in momentum, passed through the apparatus. The corrections were then fine tuned by requiring the edge position in unpolarized, i.e., spin-precessed, data to be identical for every portion of spectrometer phase space, partitioned in the above three variables. For calibration purposes, the spin-precessed data were collected at several values of spectrometer current, varying by -15% to $+5\%$ from the standard in 3% to 5% steps. The momentum resolution achieved was approximately Gaussian, with $\sigma \approx 0.13\%$.

The momentum dispersion of $1.056 \pm 0.008\%$/cm was measured in beam positron runs in which the spectrometer current was varied from 42% to 100% of the standard current in five 15% to 20% steps, and also from the edge positions found in spin-precessed runs at different settings of the spectrometer current. The uncertainty in the dispersion is based on the agreement between five calibrations which span the three data-taking runs.

V. DATA ANALYSIS

The analysis exploited the fact that near the end point the muon-decay spectrum can be expressed as a linear combination of two pure $V-A$ spectra, one with $P_\mu \cos\theta = 0$, and another with $P_\mu \cos\theta = 1$ [Sec. II, Eqs. (2.2), (2.5), and (2.6)]. The result for $\xi P_\mu \delta/\rho$ was extracted from the rate at the spectrum end point $r(\theta)$ given by Eq. (2.5).

Fitting was performed with a double-precision version of the MINUIT program,[32] and was based on minimizing the maximum likelihood Poisson statistics χ^2, defined by

$$\chi^2 = 2 \sum_i [e_i - o_i + o_i \ln(o_i/e_i)]$$

where o_i and e_i are the observed and expected number of events, respectively, for the ith bin. Section V A discusses the fitting procedure in detail.

For reasons detailed in Appendix B, the data were fitted separately in five $\cos\theta_e$ bins 0.005 wide, $0.975 \le \cos\theta_e \le 1$, where θ_e is the angle between the positron momentum and the solenoid axis. Events with $\cos\theta_e < 0.975$ were dropped from analysis since they had low statistical power. For each $\cos\theta_e$ bin the fitting proceeded in two stages. First, the spin-precessed data (Fig. 7) were fitted to calibrate the spectrometer and determine its resolution and acceptance functions. The position of the $x=1$ edge of these data fixed the momentum scale; the edge sharpness determined the momentum resolution. In the second stage, the spin-held data (Fig. 7) were fitted using the parameters found in the first fit. The result for $\xi P_\mu \delta/\rho$ was extracted from the relative rate at the end point $r(\theta)$ for the spin-held data [denoted by $r(\theta_{\rm av})$], given by Eq. (2.5):

$$r(\theta_{\rm av}) = 1 - \xi P_\mu \frac{\delta}{\rho} \cos\theta_{\rm av} \ . \tag{5.1}$$

Then the $r(\theta_{\rm av})$ from each $\cos\theta_e$ bin, with asymmetric errors, were used in a fixed slope extrapolation to $\cos\theta_{\rm av}=1$, yielding $\xi P_\mu \delta/\rho$.

$\cos\theta_{\rm av}$ was computed from $\cos\theta_\mu \cos\theta_e$ (θ_μ is the polar angle of the muon momentum) averaged over the spin-held data. Since the muon spins precessed about the solenoid axis very rapidly compared to the muon lifetime, $\cos\theta_\mu \cos\theta_e$ is equivalent to $\cos\theta$ averaged over one spin-precession period ($T \ll \tau_\mu$):

$$\cos\theta_\mu \cos\theta_e = -(1/T) \int_0^T \hat{\mathbf{s}}_\mu(t) \cdot \hat{\mathbf{p}}_e dt \ , \tag{5.2}$$

where $\hat{\mathbf{s}}_\mu$ and $\hat{\mathbf{p}}_e$ are unit vectors along the muon spin and positron momentum, respectively. However, as considered in Appendix B, $\cos\theta_{\rm av}$ is *not* equal to the data-averaged $\cos\theta$. Two small corrections, discussed in Appendixes C and D, were required.

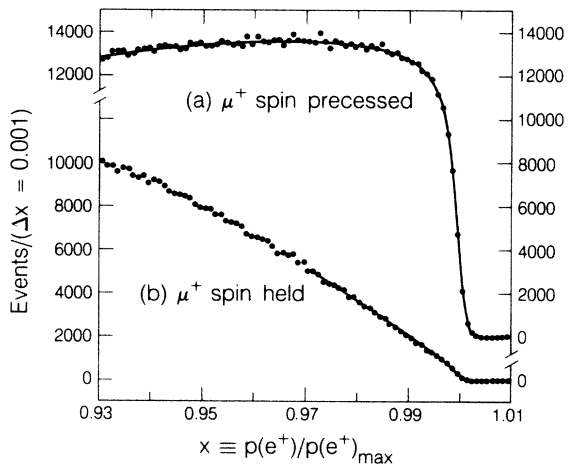

FIG. 7. Measured positron spectra for (a) spin-precessing mode and (b) spin-holding mode. x is the reduced positron momentum. The solid curves show the fitted x ranges ($x > 0.93$ for the spin-precessed and $x > 0.97$ for the spin-held data). The edge in (a) corresponds to a resolution with a Gaussian part less than 0.15% rms. The spectra shown contain the data from all targets. Fits were performed for each target separately in five $\cos\theta_e$ bins, as described in the text.

The analysis received two independent checks. First, nonstochastic positron spectra were generated numerically in the five $\cos\theta_e$ bins for various values of the muon-decay parameters ρ,δ,ξ and for various realistic angular and momentum acceptance functions. The incoming muon distribution was taken to be the measured distribution discussed in Appendix C. These spectra were then analyzed and the results for $r(\theta_{\rm av})$ were compared with the expected value $[1-(\xi P_\mu \delta/\rho)\cos\theta_{\rm av}]$, where $\cos\theta_{\rm av}$ is defined by Eq. (B5) in Appendix B. It was verified that for $\tilde{\rho}=\tilde{\delta}=0$ [$\tilde{\rho}=1-(\frac{4}{3})\rho$, $\tilde{\delta}=1-(\frac{4}{3})\delta$] the agreement between $r(\theta_{\rm av})$ and the prediction was always very precise. For nonzero $\tilde{\rho}$ and $\tilde{\delta}$ the agreement was to first order in $\tilde{\rho}$ and $\tilde{\delta}$, as expected (see Sec. II).

In the second check, the analysis was applied to data generated with a full Monte Carlo simulation of the experiment, with $\xi P_\mu \delta/\rho = 1$. Particles were moved in small steps from the vacuum window to the stopping target for μ^+, and from the stopping target to the last wire plane in the drift chamber D4 for e^+. Scattering and energy loss were applied at each step. The Monte Carlo data were processed with the same event reconstruction and selection algorithms as the experimental data. After two corrections totalling $-0.000\,23$ to $\cos\theta_{\rm av}$, the result for $\xi P_\mu \delta/\rho$ was $0.999\,92 \pm 0.000\,38$, in good agreement with the expected value of 1.

A. Fitting procedure

For the spin-precessed data, cuts on muon-decay time were adjusted to obtain a time-average unpolarized data sample. The resulting spectrum, binned in x bins 0.001 wide (see Fig. 7), was fitted from $x=0.93$ to $x=1.01$ as

$$N_1 S_{V-A}(x,0) A(x) \ , \tag{5.3}$$

where N_1 is a free normalization, and $S_{V-A}(x,0)$ is the pure $V-A$ decay spectrum with $P_\mu \cos\theta = 0$. $A(x)$ is a quadratic acceptance function given by

$$A(x) = 1 + B_1(1-x) + B_2(1-x)^2 \ , \tag{5.4}$$

with the coefficients B_1 and B_2 also free in the fit.

If $\tilde{\rho}$ is nonzero the unpolarized spectrum in x does not match the unpolarized $V-A$ spectrum $S_{V-A}(x,0)$, and the acceptance function (5.4) will absorb the difference in shapes. Then B_1 in Eq. (5.4) shifts by $+6\tilde{\rho}$, and B_2 by $(6B_1-12)\tilde{\rho}$. Fortunately, an error in B_1 (B_2) propagates into an error in $\xi P_\mu \delta/\rho$ with a factor of 10^{-3} (1.5×10^{-5}), and this effect can be ignored.

The fitting function (5.3) was smeared to reflect spectrometer resolution and positron energy-loss straggling. Bhabba scattering and bremsstrahlung were modeled in the 23 to 170 mg/cm^2 of residual target and $\approx$200 mg/cm^2 of other material between the muon-decay point and the spectrometer vacuum tank window. The spectrometer resolution in x was parametrized by a normalized sum of three Gaussians with standard deviations σ, $\sqrt{3}\sigma$, and 3σ. The $\sqrt{3}\sigma$ and 3σ Gaussians were introduced in order to obtain a better fit to the tails of the resolution, and they usually had small coefficients in the normalized sum. The resolution σ was typically 0.13%. The result for $\xi P_\mu \delta/\rho$ was relatively insensitive to the number

of free parameters in the resolution function, changing by less than 10^{-4} when a single Gaussian was used rather than all three.

In summary, the seven free parameters used to fit the spin-precessed data were the normalization N_1, the acceptance coefficients B_1 and B_2, the three resolution parameters, and the position of the $x=1$ point on the reconstructed momentum scale.

Despite the large momentum acceptance of the apparatus, the spin-precessed data were fitted only from $x=0.93$ and the spin-held data only from $x=0.97$. A short extension of the x range below $x=0.93$ for the spin-precessed data had no effect on the result for $\xi P_\mu \delta/\rho$. A significant extension would have required more free parameters to fit the acceptance, and would not have led to a decrease in the statistical error on $\xi P_\mu \delta/\rho$. Similarly, the extension of the x range below 0.97 for the spin-held data would have required introducing a free parameter to represent a possible difference in acceptance between the spin-precessed and spin-held data sets. The associated systematic error increased quadratically with the fit range, offsetting the improvement in the statistical error. The range $x \geq 0.97$ was optimal for the smallest combined statistical and systematic error.

The spin-held data (Fig. 7) were fit using the values for the x acceptance, x resolution, and $x=1$ calibration point of the spin-precessed data. In this second stage of fitting the two data sets were fit simultaneously to allow the uncertainties in the $x=1$ calibration and x acceptance to contribute ($\approx 3\%$ of the error) to the statistical error on $\xi P_\mu \delta/\rho$. Since the resolution in x was determined primarily by the sharpness of the $x=1$ edge in the spin-precessed data, the resolution parameters in the combined fit were fixed to the values found when the spin-precessed data were fitted alone. This simplification did not affect the result or the errors on $\xi P_\mu \delta/\rho$, while speeding the analysis by a factor of 3. The form of the spin-held data was taken to be [Eq. (2.2)]

$$N_2\{[1-r(\theta_{\rm av})]S_{V-A}(x,1)+r(\theta_{\rm av})S_{V-A}(x,0)\}A(x)\ , \tag{5.5}$$

where N_2 is a free normalization, $S_{V-A}(x,1)$ and $S_{V-A}(x,0)$ are the pure $V-A$ spectra at $P_\mu \cos\theta=1$ and $P_\mu \cos\theta=0$, respectively, $A(x)$ is the quadratic acceptance function (5.4), and the free parameter $r(\theta_{\rm av})$ is the relative rate at the end point. The function (5.5) was smeared in the same manner as for the spin-precessed data to reflect the spectrometer resolution and positron energy-loss straggling.

In summary, the six free parameters in the combined fit were the $x=1$ calibration point, N_1, B_1, B_2 (all determined primarily by the spin-precessed data), and N_2 and $r(\theta_{\rm av})$ (determined by the spin-held data).

B. Corrections

One correction, due to muon depolarization from electron scattering while stopping, was made directly to the result (see Appendix E). Two other corrections were made to $\cos\theta_{\rm av}$ as computed from the data-averaged $\cos\theta_\mu \cos\theta_e$. Adding a correction to $\langle \cos\theta_\mu \cos\theta_e \rangle$ is equivalent to reducing $\xi P_\mu \delta/\rho$ by the same amount. The corrections and their uncertainties are listed in Table II.

The two corrections to $\cos\theta_{\rm av}$ are motivated by the discussion in Appendix B. Here we merely note their origin. The first correction was for the difference between $\langle \cos\theta_\mu \cos\theta_e \rangle$ computed from the measured tracks, and $\langle \cos\theta_\mu \cos\theta_e \rangle$ if it were computed from the true values of θ_μ and θ_e (Appendix C). The difference was due mostly to Coulomb scattering, although finite chamber resolution also contributed. This target-dependent correction varied from -0.0007 to 0.0002, with a target-averaged value of -0.0001. The second correction was for the difference between the mean acceptance angle as calculated from the decay-biased data [$\langle \cos\theta_\mu \cos\theta_e \rangle$ given by Eq. (B6) in Appendix B], and as calculated purely from the acceptance of the apparatus [$\cos\theta_{\rm av}$ defined by (B5)]. This correction is discussed in detail in Appendix D.

C. Results of fits

All of the data were used in the analysis, with the exception of runs which had some known deficiency (e.g., too low a voltage on the drift-chamber wire planes). The fitted $\xi P_\mu \delta/\rho$ for all targets in the three data-taking runs are plotted in Fig. 8, where only statistical errors are

TABLE II. Corrections to $\cos\theta_{\rm av}$ and $\xi P_\mu \delta/\rho$ and estimated possible systematic errors in the corrections. Adding a correction to $\cos\theta_{\rm av}$ is equivalent to reducing $\xi P_\mu \delta/\rho$ by the same amount.

Corrections	Values	Errors
Correction to $\xi P_\mu \delta/\rho$ due to muon depolarization in scattering with unpolarized electrons	+0.0007	<0.0001
Correction (averaged over all targets) to $\cos\theta_{\rm av}$ due to Coulomb scattering and finite chamber resolution	−0.0001	±0.0003
Correction to $\cos\theta_{\rm av}$ due to use of data averaged $\cos\theta_\mu \cos\theta_e$	+0.0001	<0.0001

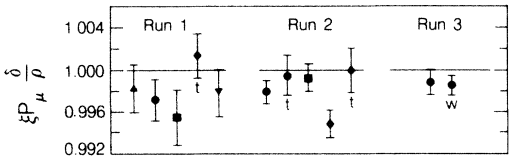

FIG. 8. Results for $\xi P_\mu \delta/\rho$ for each target in the three data-taking runs (denoted by run 1, etc.). Only statistical errors are shown. The targets are Ag (triangles), Al (circles), Au (squares), Cu (diamonds), and He (inverted triangles). The spin-holding field was 0.3 T for the target marked by w and 1.1 T for the other targets. The thicker targets are marked by t. Target thicknesses are compiled in Appendix A.

shown. The systematic errors will be considered in Sec. VI. The plotted values include the three corrections just discussed.

It was discovered during run 2 that the thinner of the two Cu targets was not sufficiently thick to stop all muons. The amount of material beyond the mean muon-stopping range is estimated to be only 2.5 straggling lengths for this target. The fitted $\xi P_\mu \delta/\rho$ for this target is significantly lower (3.0σ) than the combined result from all other targets (see Table III), and also lower than the combined result from the thicker Cu targets (4.6σ). Since the $\approx 0.6\%$ of the muons which leaked out of the target could have been depolarized in air or in the Mylar window of P3, we have chosen not to include this target in the computation of the combined result for $\xi P_\mu \delta/\rho$.

The values of $\xi P_\mu \delta/\rho$ for each metal, liquid He, and all targets together are tabulated in Table III (the thinner Cu target in run 2 is excluded; only statistical errors are listed). We note that in our analysis of the spin-precessed data using the muon-spin-rotation (μSR) technique,[12] He was found to be 12% depolarizing. The depolarization was most likely due to muonium formation (Sec. III C). If so, the suppression of muon depolarization in muonium by the 1.1-T longitudinal field would explain the difference between the two results.

The results for all targets were combined for each of the $\cos\theta_e$ bins, and are plotted in Fig. 9 as

TABLE III. Measured $\xi P_\mu \delta/\rho$ for each metal, liquid He and all targets combined. Only statistical errors are shown.

Material	$\xi P_\mu \delta/\rho$
Ag	$0.9983^{+0.0022}_{-0.0023}$
Al	$0.9985^{+0.00056}_{-0.00056}$
Au	$0.9986^{+0.0011}_{-0.0011}$
Cu	$1.0007^{+0.0015}_{-0.0015}$
He	$0.9979^{+0.0022}_{-0.0023}$
All targets	$0.9986^{+0.00046}_{-0.00046}$

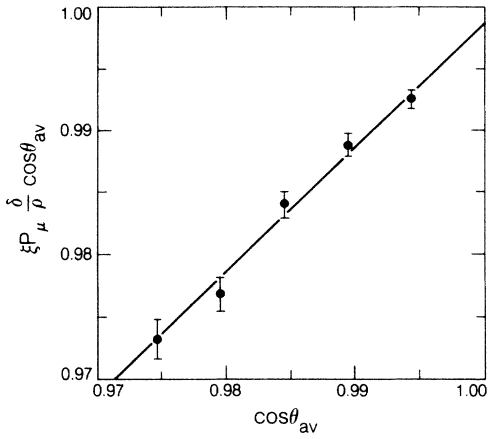

FIG. 9. Results for $(\xi P_\mu \delta/\rho)\cos\theta_{av}$ from the five $\cos\theta_e$ bins plotted vs $\cos\theta_{av}$. Only statistical errors are shown. The corrections discussed in Sec. V B have been incorporated. The fitted straight line indicates the fixed slope extrapolation to $\cos\theta_{av}=1$.

$$\xi P_\mu \frac{\delta}{\rho}\cos\theta_{av} = 1 - r(\theta_{av})$$

vs $\cos\theta_{av}$. The corrections discussed in Section V B are included. Again, only statistical errors are shown. The fitted straight line in Fig. 9 exhibits the fixed slope extrapolation to $\cos\theta_{av}=1$.

Using 93% of the data—representing the Al, Au, and Cu targets (including the thinner run 2 Cu target)—the results for $\xi P_\mu \delta/\rho$ were also evaluated over four muon-decay time ranges. The ranges chosen were 0.1—0.85, 0.85—2.1, 2.1—5.1, and 5.1—10 μsec after the muon ar-

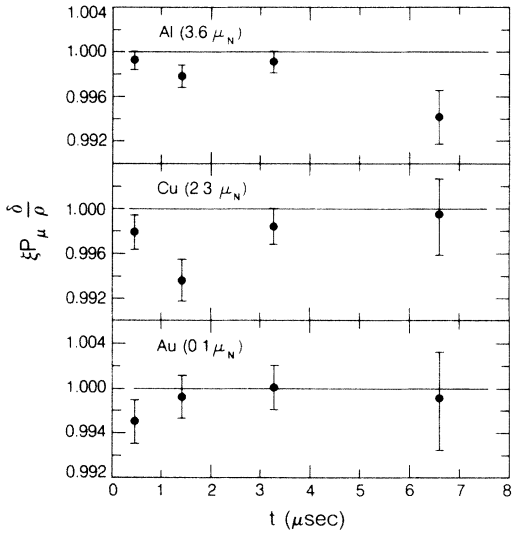

FIG. 10. The results for $\xi P_\mu \delta/\rho$ evaluated in four muon-decay time ranges for the three metal targets, Al, Cu, and Au, constituting 93% of the data. Only statistical errors are shown. The results are plotted vs t, given by Eq. (5.6). The target material nuclear magnetic moment in units of nuclear magnetons (μ_N) is indicated. Only the results for Al are suggestive of a time-dependent spin relaxation.

rival. The stopped muon polarization is expected to decay exponentially (Sec. III C) with characteristic spin-lattice relaxation time constant T_1 toward an equilibrium in which the numbers of muon spins parallel or antiparallel to the field are almost equal. If $T_1 \gg 10$ μsec, the fitted $\xi P_\mu \delta/\rho$ will depend linearly on the quantity

$$t = t_1 + \tau_\mu - (t_2 - t_1)\{\exp[(t_2 - t_1)/\tau_\mu] - 1\}^{-1}, \quad (5.6)$$

where t_1 and t_2 are the start and end of a time range. As can be seen in Fig. 10, only the Al data suggest a time-dependent spin relaxation. If the spin relaxation is caused by nuclear magnetic dipole moments, the relaxation times for Al, Cu, and Au should correlate with their respective dipole moments of 3.6, 2.3, and 0.1 nuclear magnetons. The fitted slope of $(-4.3\pm3.4)\times10^{-4}$ μsec^{-1} for Al corresponds to $T_1 = 4.6$ msec, which would imply that a correction of $(+9.9\pm7.8)\times10^{-4}$ should be added to the result for $\xi P_\mu \delta/\rho$ for Al. Contrary to the expectation based on the result for Al, the best-fit slope for Cu is actually positive $[(+4.5\pm4.8)\times10^{-4}$ μsec]. Since our result will be used to set a lower limit on $\xi P_\mu \delta/\rho$, we have conservatively chosen not to apply a spin-relaxation correction.

VI. SYSTEMATIC ERRORS

The possible sources of systematic errors larger than 1×10^{-4} are summarized in Table IV. In principle they should be uncorrelated, and add in quadrature to $\pm7.5\times10^{-4}$. The systematic error in the scattering correction is discussed in Appendix C. The remaining systematic errors will be considered below.

A. End-point calibration

Recall that the absolute momentum calibration was determined from the $x = 1$ edge position in the spin-precessed data (Sec. V A). In both the first (spin-precessed) and second (combined) stages of fitting, the position of the $x = 1$ point on the reconstructed momentum scale was a free parameter, although it was assumed to be identical for the spin-held and spin-precessed data sets. However, the strong longitudinal field in the target region for the spin-held data might have induced a small difference by slightly changing the distribution of trajectories in the spectrometer magnet. Possible imperfections in the momentum reconstruction algorithm could then lead to a calibration difference. In principle, the difference could be calculated from the detailed Monte Carlo simulation of the experiment, except that the small deviations from cylindrical symmetry in the true spectrometer field were not incorporated in the simulation. We must therefore rely on the data to establish a limit.

We denote by $x_{1,\mathrm{sh}}$ the reconstructed position of the $x = 1$ point for the spin-held data, and by $x_{1,\mathrm{sp}}$ the spin-precessed point. The difference in $x = 1$ calibration points is then $\Delta x_1 = x_{1,\mathrm{sh}} - x_{1,\mathrm{sp}}$. Already $x_{1,\mathrm{sp}}$ was known from the first stage of fitting. Then $x_{1,\mathrm{sh}}$ was determined by fitting the spin-held data according to (5.5), but leaving the $x = 1$ position as a free parameter. To increase the statistical power of this fit, the cut to eliminate cloud muons was not applied.

The mean Δx_1 averaged over all five $\cos\theta_e$ bins and all targets was found to be $(0.17\pm0.45)\times10^{-4}$ ($\chi^2 = 36$ for 54 degrees of freedom). The slope in Δx_1 vs $\cos\theta_e$ was consistent with zero (0.0010 ± 0.0066), and hence Δx_1 was assumed to be the same for all $\cos\theta_e$ bins. Analysis shows that shifting the spin-held data by Δx_1 changes $\xi P_\mu \delta/\rho$ by Δx_1. Since our result will be used to set a lower limit on $\xi P_\mu \delta/\rho$, we conservatively chose not to correct for the positive central value of Δx_1. However, a systematic error of $\pm3.5\times10^{-4}$ was assigned to $\xi P_\mu \delta/\rho$.

B. Momentum acceptance

The acceptance in reduced positron momentum x, which was assumed to be the same for the spin-held and spin-precessed data, might also differ slightly because of the strong longitudinal field in the target region. Let $D(x)$ describe the possible difference in x acceptance between the two data sets. As the normalization was a free parameter in the fit, we take $D(1) = 1$. The lowest-order (linear) term in $D(x)$ may be estimated by extending the range of the spin-held fit from $x_{\min} = 0.97$ to $x_{\min} = 0.93$, and multiplying the fitting function for the spin-held data [Eq. (5.5)] by $D(x) = 1 + D_1(x - 1)$. After averaging over the five $\cos\theta_e$ bins and all targets, the fitted D_1 was 0.14 ± 0.18 ($\chi^2 = 44$ for 54 degrees of freedom). The slope

TABLE IV. Possible sources of systematic error $\geq 1\times10^{-4}$ and their estimated contributions.

Sources of possible error	Errors
Coulomb scattering correction	±0.000 3
Difference in $x = 1$ calibration (±0.000 35) and x acceptance (±0.0002) between the spin-held and spin-precessed data	±0.000 55
Spectrometer momentum dispersion	±0.000 1
Uncertainty in the longitudinal position of wire planes for chambers near the target	±0.000 25
Accuracy of $\cos\theta_\mu$ and $\cos\theta_e$ reconstruction using first-order optics approximation	±0.000 25
Total 1σ possible error	±0.000 75

versus $\cos\theta_e$ was consistent with zero (7 ± 27), so D_1 was taken to be the same for all $\cos\theta_e$ bins. When $D(x)$ was used in the fit of the spin-held data, the result for $\xi P_\mu\delta/\rho$ changed by $0.001 D_1$, while the rate of change in $\xi P_\mu\delta/\rho$ with D_1 varied quadratically with $(1-x_{\min})$. The smallest combined (statistical and systematic) error was obtained with $x_{\min}=0.97$.

As with the $x=1$ calibration error, we conservatively chose not to make the upward correction to $\xi P_\mu\delta/\rho$ that was indicated by the positive central value of D_1, and only a systematic error of $\pm2\times10^{-4}$ was assigned. Since the possible differences in the $x=1$ calibration and x acceptance are both due to the longitudinal field in the target region, the two errors were combined in sum in the computation of the total systematic error.

C. Momentum dispersion

The spectrometer momentum dispersion was measured to be $(1.056\pm0.008)\%$/cm (Sec. IV). If, for example, the true dispersion were less, the reconstructed reduced positron momentum x would be shifted closer to 1. Thus a decrease in dispersion could be parametrized by a factor $\lambda(\lambda<1)$ by which the reconstructed momentum scale is compressed towards $x=1$.

The spin-held data are given approximately by a linear function vanishing at $x=1$ plus a constant. Therefore, when the x scale is compressed by a factor λ, the normalization parameter N_2 in the fitting function for the spin-held data [Eq. (5.5)] increases by a factor of $\approx1/\lambda^2$. Near $x=1$ the number of events per x bin increases by a factor of $1/\lambda$. Since this number is proportional to $N_2 r(\theta_{\rm av})$, where $r(\theta_{\rm av})$ is the relative rate at the end point, $r(\theta_{\rm av})$ decreases by a factor of λ, as was verified in the analysis. Since $\xi P_\mu\delta/\rho$ was extracted from $r(\theta_{\rm av})=1-(\xi P_\mu\delta/\rho)\cos\theta_{\rm av}$, with a mean $r(\theta_{\rm av})$ of 0.015, a systematic error of $\pm1\times10^{-4}$ was assigned to $\xi P_\mu\delta/\rho$ from this source.

D. Reconstruction of $\cos\theta_\mu$ and $\cos\theta_e$

There are two more sources of possible systematic error in the reconstruction of $\cos\theta_\mu$ and $\cos\theta_e$, in addition to the systematic error in the scattering correction to $\langle\cos\theta_\mu\cos\theta_e\rangle$ (Sec. VI A). First we consider the uncertainties in the longitudinal positions of the wire planes in the proportional chambers near the target. We denote by $\Delta\cos\theta_\mu$ the difference between $\langle\cos\theta_\mu\rangle$ (i.e., the data-averaged $\cos\theta_\mu$) if it were computed from the true angles and $\langle\cos\theta_\mu\rangle$ computed from the measured angles. Similarly, $\Delta\cos\theta_e$ denotes the same difference for positrons. The uncertainty of ±2 mm in the longitudinal distance between the proportional chambers P1 and P2 (see Fig. 3) leads to a systematic error of $\pm2\times10^{-4}$ in $\Delta\cos\theta_\mu$, and consequently in $\xi P_\mu\delta/\rho$. The uncertainty of ±2 mm in the longitudinal position of the proportional chamber P3 with respect to the drift chambers D1 and D2 leads to a systematic error of $\pm1.5\times10^{-4}$ in $\Delta\cos\theta_e$. These errors combine in quadrature to $\pm2.5\times10^{-4}$.

Second, we consider the systematic error due to the first-order optics approximation used in the fit of curved tracks in the solenoid (Sec. IV). From the full Monte Carlo simulation of the polarimeter it was found that, in the absence of scattering and chamber resolution effects, $\Delta\cos\theta_\mu=+2\times10^{-6}$ and $\Delta\cos\theta_e=-2\times10^{-5}$. Hence, the accuracy of the first-order optics approximation in determining $\cos\theta_\mu$ and $\cos\theta_e$ is assumed to be better than $\pm1\times10^{-4}$. However, a systematic error of $\pm2.5\times10^{-4}$ was assigned to $\xi P_\mu\delta/\rho$ owing to uncertainty in the solenoid field map used in the track fit.

VII. DISCUSSION AND CONCLUSIONS

A. Limit on $\xi P_\mu\delta/\rho$

Since we are unable to correct for all possible sources of muon depolarization in the stopping target, we quote our result as a lower limit for $\xi P_\mu\delta/\rho$. Accordingly, we did not apply the possible upward corrections to $\xi P_\mu\delta/\rho$ discussed in Secs. V C, VI A, and VI B. Without these corrections, the combined result from all stopping targets

$$\xi P_\mu\delta/\rho=0.998\,63\pm0.000\,46(\text{stat})\pm0.000\,75(\text{syst})$$

is still fairly consistent (1.6σ) with the $V-A$ prediction of unity. Excluding the unphysical region ($\xi P_\mu\delta/\rho>1$), the 90% confidence limit is

$$\xi P_\mu\delta/\rho>0.997\,47\ .$$

The result is in agreement with the 90% confidence limit

$$\xi P_\mu\delta/\rho>0.9951$$

obtained in the analysis of the spin-precessed data using the muon-spin-rotation technique.[11,12] The two methods of analysis have different major sources of possible systematic error, and it is therefore appropriate to combine the two results as independent measurements:

$$\xi P_\mu\delta/\rho>0.997\,53\ . \tag{7.1}$$

This combined 90% confidence limit will be used to draw our conclusions.

B. Limits on right-handed currents with massless neutrinos

From Eq. (2.7) it is seen that our result (7.1) constrains both ϵ and ζ. The contour corresponding to the 90% confidence limit on ϵ and ζ is plotted in Fig. 1. Assuming $m(W_1)=81$ GeV/c^2, 90% confidence limits for the following special cases are obtained: $m(W_2)>514$ GeV/c^2 for $\zeta=0$ and $m(W_2)>432$ GeV/c^2 when ζ is unconstrained; $|\zeta|<0.035$ for $m(W_2)=\infty$ and $-0.050<\zeta<0.035$ when $m(W_2)$ is unconstrained.

Herczeg[33] has obtained the expression for $(1-\xi P_\mu\delta/\rho)$ for a general left-right-symmetric (LRS) theory, assuming that neutrinos are either sufficiently light that their effect on the spectrum can be ignored, or that they are too heavy to be produced in muon decay. In addition to ϵ and ζ, the general expression, which we do not reproduce here, contains the left-handed and right-handed weak coupling constants, the left-handed and right-handed quark mixing angles, the *CP*-violating phase in W-W mixing, the mixing angles for neutrinos, and a *CP*-violating phase from the quark sector. For a general LRS theory, constraints

that are obtained from the limit on $\xi P_\mu \delta/\rho$ depend on the assumptions one makes about the values of these parameters.

C. Limits on $m(\nu_{\mu L})$ and $\nu_{\mu L}$ helicity in π^+ decay

Equation (7.1) implies limits on the mass of the left-handed muon neutrino and its helicity in pion decay. The weakest limits are obtained if it is assumed that right-handed currents are absent. In that case $\xi\delta/\rho=1$ and hence $P_\mu > 0.9975$. The 90% confidence limit on the $\nu_{\mu L}$ helicity in π^+ decay is therefore $h(\nu_{\mu L} < -0.9975$. The corresponding limit on the $\nu_{\mu L}$ velocity ($\beta > 0.9975$) in π^+ decay implies the 90% confidence limit $m(\nu_{\mu L}) < 2.1$ MeV/c^2. For comparison the world-average value[21] $m(\nu_{\mu L}) < 0.5$ MeV/c^2 implies $P_\mu > 0.999\,86$ in the absence of right-handed currents.

D. Restrictions on the Lorentz structure of leptonic charged weak interactions

Mursula and Scheck[2] have recently obtained limits on non-($V-A$) weak couplings using a helicity projection form of the flavor retention contact interaction Hamiltonian:

$$\begin{aligned} H=(G_0/\sqrt{2})[&h_{11}(s+p)_{e\nu_e}(s+p)_{\nu_\mu\mu}+h_{12}(s+p)(s-p)+h_{21}(s-p)(s+p)\\ &+h_{22}(s-p)(s-p)+g_{11}(v^\alpha+a^\alpha)(v_\alpha+a_\alpha)+g_{12}(v^\alpha+a^\alpha)(v_\alpha-a_\alpha)\\ &+g_{21}(v^\alpha-a^\alpha)(v_\alpha+a_\alpha)+g_{22}(v^\alpha-a^\alpha)(v_\alpha-a_\alpha)\\ &+f_{11}(t^{\alpha\beta}+t'^{\alpha\beta})(t_{\alpha\beta}+t'_{\alpha\beta})+f_{22}(t^{\alpha\beta}-t'^{\alpha\beta})(t_{\alpha\beta}-t'_{\alpha\beta})+\text{H.c.}]\,, \end{aligned} \tag{7.2}$$

where $s_{ik}=\bar\psi_i 1\psi_k$, $p_{ik}=\bar\psi_i\gamma_5\psi_k$, $v^\alpha_{ik}=\bar\psi_i\gamma^\alpha\psi_k$, $a^\alpha_{ik}=\bar\psi_i\gamma^\alpha\gamma_5\psi_k$, $t^{\alpha\beta}_{ik}=\bar\psi_i(\sigma^{\alpha\beta}/\sqrt{2})\psi_k$, $t'^{\alpha\beta}_{ik}=\bar\psi_i(\sigma^{\alpha\beta}\gamma_5/\sqrt{2})\psi_k$ and the particle indices are as indicated in the h_{11} term.

There are several advantages to using a Hamiltonian of this form. For a pure $V-A$ interaction only g_{22} is nonzero ($g_{22}=1$) while all other coupling constants vanish. Also, in the limit of massless particles the combinations of covariants in each term of Eq. (7.2) project onto states of definite helicity. As a consequence, the number of interference terms in any decay rate is minimal since only scalar-pseudoscalar and tensor terms interfere.

Several constraints are imposed on coupling constants in the models[2] with "factorization and universality," where it is assumed that (i) the charged weak interactions are mediated by a single heavy boson with spin 0, 1, or 2, (ii) V,A,T couplings are $e-\mu$ universal, but (iii) scalar and pseudoscalar coupling constants can be proportional to the charged-lepton mass:

$$\begin{aligned} &h_{12},\ h_{21} \text{ real, positive semidefinite};\\ &h_{22}=h_{11}^* \text{ with } |h_{11}|^2=h_{12}h_{21};\\ &g_{11},\ g_{22} \text{ real, positive semidefinite};\\ &g_{21}=g_{12}^* \text{ with } |g_{12}|^2=g_{11}g_{22};\\ &f_{22}=f_{11}^*\,. \end{aligned} \tag{7.3}$$

In terms of the coupling constants in Eq. (7.2) the deviation of $\xi\delta/\rho$ from the $V-A$ value of 1 is given by

$$1-\xi\delta/\rho=\frac{8|g_{11}|^2+2|h_{21}|^2+2|h_{11}-2f_{11}|^2}{4(|g_{11}|^2+|g_{22}|^2)+|h_{12}|^2+|h_{21}|^2+|h_{11}-2f_{11}|^2+|h_{22}-2f_{22}|^2}\,.$$

Hence the measurement of $\xi P_\mu\delta/\rho$ sets limits on g_{11}, h_{11}, h_{21}, and f_{11}. The weakest limits are obtained if it is assumed that the couplings responsible for μ^+ decay are unrelated to π^+ decay couplings. In this case the value of P_μ cannot be expressed in terms of the couplings in (7.2), and hence the limits are obtained from $\xi\delta/\rho \geq \xi P_\mu\delta/\rho$. If only one coupling other than the $V-A$ coupling $g_{22}=1$ is nonzero the 90% confidence limit $\xi\delta/\rho > 0.9975$ restricts $|g_{11}|$ or $|f_{11}| < 0.035$ and $|h_{11}|$ or $|h_{21}| < 0.070$. Stronger limits on the couplings can be obtained with assumptions of weak-interaction universality. In the model with manifest left-right symmetry and no left-right mixing, for example, $P_\mu = 1-2|g_{11}|^2/|g_{22}|^2$ to lowest order in g_{11}, and hence a 90% confidence limit on the $V+A$ coupling g_{11} is $|g_{11}| < 0.025$. The limits on g_{11}, f_{11}, h_{11}, and h_{21} in turn provide constraints on other couplings (e.g., f_{22},h_{22}) in models with factorization and universality, due to relations (7.3).

Although (7.1) constrains the pure $V+A$ coupling g_{11}, it does not constrain the couplings g_{12} and g_{21}, corresponding to the $V-A$ coupling at one vertex ($e\nu_e$ or $\mu\nu_\mu$), but $V+A$ coupling at the other vertex. These couplings are constrained by the muon-decay parameter ρ:

$$\rho-\tfrac{3}{4}=-(12/A)[|g_{12}|^2+|g_{21}|^2+2|f_{11}|^2+2|f_{22}|^2+\text{Re}(h_{11}f_{11}^*+h_{22}f_{22}^*)]\,,$$

where

$$A=4[4(|g_{22}|^2+|g_{11}|^2+|g_{12}|^2+|g_{21}|^2)+|h_{11}|^2+|h_{12}|^2+|h_{21}|^2+|h_{22}|^2+12(|f_{11}|^2+|f_{22}|^2)]\,.$$

Assuming that only g_{12} and g_{21} couplings are nonzero in addition to the $V-A$ coupling $g_{22}=1$, the world-average value[21] of $\rho=0.7517\pm0.0026$ implies the 90% confidence limit

$$(|g_{12}|^2+|g_{21}|^2)<0.0045$$

when the unphysical region ($\rho>\frac{3}{4}$) is excluded.

E. Limits on composite leptons

The possibility that leptons and quarks are composite at some mass scale Λ has received considerable attention in recent years. Among the strongest experimental limits on Λ currently quoted[34] are those from the deviation of the muon gyromagnetic ratio g from 2 (>860 GeV), ν-hadron scattering (>2.5 TeV), Bhabha scattering (1—3 TeV), and the reaction $e^+e^-\to\mu^+\mu^-$ (2—3.5 TeV).

The effects of compositeness may be analyzed in terms of new effective contact interactions. Following the analyses of Peskin,[35] and Lane and Barany[36] the most general SU(2)×U(1)-invariant contact interaction contributing to $\mu\to e\bar{\nu}\nu$ is

$$\begin{aligned}L_{\text{cont}}=(g^2/\Lambda^2)[&\eta_1(\bar{\nu}_{\mu L}\gamma^\kappa\mu_L)(\bar{e}_L\gamma_\kappa\nu_{eL})+\eta_2(\bar{\nu}_{\mu R}\gamma^\kappa\mu_R)(\bar{e}_R\gamma_\kappa\nu_{eR})+\eta_3(\bar{\nu}_{\mu L}\gamma^\kappa\nu_{eL})(\bar{e}_R\gamma_\kappa\mu_R)+\eta_4(\bar{e}_L\gamma^\kappa\mu_L)(\bar{\nu}_{\mu R}\gamma_\kappa\nu_{eR})\\&+\eta_5(\bar{\nu}_{\mu L}\mu_R)(\bar{e}_L\nu_{eR})+\eta_6(\bar{\nu}_{\mu L}\nu_{eR})(\bar{e}_L\mu_R)+\eta_7(\bar{\nu}_{\mu R}\mu_L)(\bar{e}_R\nu_{eL})+\eta_8(\bar{\nu}_{\mu R}\nu_{eL})(\bar{e}_R\mu_L)]\,,\end{aligned}\tag{7.4}$$

where g is a coupling of hadronic strength; the η_i are usually assumed to be of order unity and are normalized so that $|\eta_L|=1$ in the diagonal coupling

$$(g^2/2\Lambda^2)[\eta_L(\bar{e}_L\gamma^\kappa e_L)(\bar{e}_L\gamma_\kappa e_L)+\cdots]\,.$$

The first and second terms in Eq. (7.4) are purely left and right handed, respectively, and hence are indistinguishable from the usual $V-A$ and $V+A$ interactions.

There are three special cases of interest.

(1) If only left-handed (right-handed) leptons are composite then only the purely left-handed (right-handed) term survives, i.e., only η_1 (η_2)$\neq0$.

(2) If both left- and right-handed leptons are composite but contain quite different sets of constituents then the purely left- and right-handed terms dominate, i.e., $\eta_1,\eta_2\gg$other η_i.

(3) If there is no ν_R, or $m(\nu_R)$ is large, only $\eta_1,\eta_3\neq0$.

Assuming an effective interaction Lagrangian $L_{\text{eff}}=L_{V-A}+L_{\text{cont}}$ we obtain the end-point decay rate:

$$1-\xi P_\mu\delta/\rho=2(620\text{ GeV}/\Lambda)^4(g^2/4\pi)^2(\eta_2^2+\eta_3^2+\eta_5^2/4)\,.$$

The limit $\xi P_\mu\delta/\rho>0.9975$ then implies

$$\Lambda^2>(3310\text{ GeV})^2(g^2/4\pi)(\eta_2^2+\eta_3^2+\eta_5^2/4)^{1/2}$$

with 90% confidence. (If the not unreasonable assumptions $g^2/4\pi\approx2.1$ and $\eta_i>0.2$ are made, the limit $\Lambda>2600$ GeV is obtained.)

For the special cases discussed earlier the limit becomes (1) only left-handed leptons composite—no limit, only right-handed leptons composite—$\Lambda^2>(3310\text{ GeV})^2(g^2/4\pi)\eta_2$, (2) left- and right-handed leptons have different sets of constituents—$\Lambda^2>(3310\text{ GeV})^2(g^2/4\pi)\eta_2$, and (3) no ν_R or $M(\nu_R)$ large—$\Lambda^2>(3310\text{ GeV})^2(g^2/4\pi)\eta_3$.

F. Limits on familons

Wilczek[37] has suggested that the absence of large CP invariance violations in strong interactions could be explained by a group of genuine flavor symmetries of the Lagrangian. Spontaneous breakdown of family symmetries leads to characteristic neutral massless Nambu-Goldstone bosons called familons. The coupling of familons at low energies is described by effective Lagrangians of the type

$$\Delta L=F^{-1}j_\lambda\partial^\lambda f\,,$$

where F is the energy scale at which the flavor symmetry is spontaneously broken, f is the familon field, and j_λ is the appropriate current. Arguments based on cosmology suggest that $10^9<F<10^{12}$ GeV.

Familons may be detected by observing rare decay modes, in particular muon decay $\mu^+\to e^++f$ with the branching ratio given by

$$b_{ef}=\frac{\Gamma(\mu\to ef)}{\Gamma(\mu\to e\bar{\nu}\nu)}=\frac{2.5\times10^{14}\text{ GeV}^2}{F_{\mu e}^2}\,.\tag{7.5}$$

Since the familon is essentially massless, the decay mode $\mu\to ef$ would be revealed by a spike at the end point of the positron energy spectrum. Because the positron direction cannot be correlated with the muon spin, for a parity-conserving effective Lagrangian of the type assumed in Ref. 37, the familon would be emitted isotropically and its signature would appear most strongly in the spin-held data, where the background from normal muon decay is smaller (Fig. 7). The absence of such a spike allows us to obtain a limit on the branching ratio b_{ef} (7.5) and accordingly on the energy scale $F_{\mu e}$ at which the flavor symmetry is broken.

The fitting procedure for the computation of the branching ratio b_{ef} was essentially identical to that described in Sec. V A. The decay rate $\mu\to ef$ was added to the fitting function (5.5) for the spin-held data, but could be neglected in the fitting function for the spin-precessed data. The best-fit branching ratio is $(0.3\pm1.1)\times10^{-6}$. The effects discussed in Sec. VI contribute a possible systematic error of $\pm0.9\times10^{-6}$, with the largest contribution ($\pm0.8\times10^{-6}$) due to a possible difference in $x=1$ calibration between the spin-held and spin-precessed data sets. If the unphysical region ($b_{ef}<0$) is ignored, we obtain the 90% confidence limits

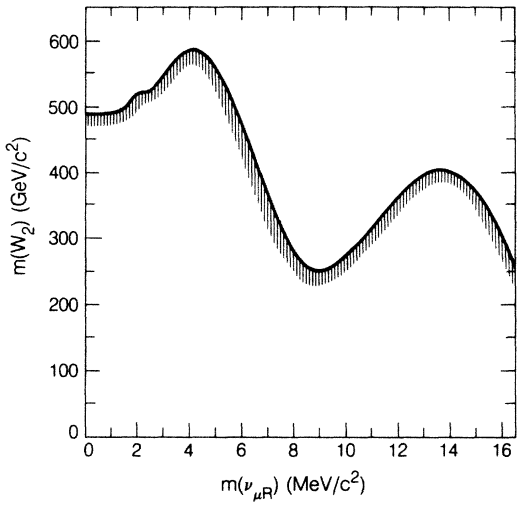

FIG. 11. Approximate limits on $m(W_2)$ versus $m(\nu_{\mu R})$ assuming $m(\nu_{eR})<1$ MeV/c^2, no mixing for neutrinos and no mixing for the gauge bosons W_1 and W_2. The allowed region lies above the contour. The computation of the limits is described in Appendix F.

$$b_{ef}<2.6\times10^{-6}$$

and

$$F_{\mu e}>9.9\times10^{9}\ \text{GeV}\ .$$

G. Limits on $m(W_2)$ with $m(\nu_{\mu R})\neq0$

If neutrinos are Majorana particles the left- and right-handed neutrinos may have different masses. As yet only massless or very light neutrinos have been considered. In the most general case the limit on $m(W_2)$ that can be extracted from the data depends on the masses of the right-handed neutrinos, on neutrino mixing angles, and on the mixing angle ζ for W_1 and W_2. Here we present approximate limits on $m(W_2)$ for a particular case of massive Majorana neutrinos. We will assume a massive $\nu_{\mu R}$ [$m(\nu_{\mu R})<16.5$ MeV/c^2], a very light ν_{eR} [$m(\nu_{eR})<1$ MeV/c^2], and manifest left-right symmetry. For simplicity we will also assume that there is no mixing between W_1 and W_2 ($\zeta=0$) or between neutrinos. The computation of the limits is described in Appendix F. The limits on $m(W_2)$ are accurate only to $\approx2\%$ because radiative corrections have not been computed for the spectrum with massive neutrinos, and also because of several simplifications in the treatment of systematic errors.

The approximate limits on $m(W_2)$ versus $m(\nu_{\mu R})$, computed assuming $m(W_1)=81$ GeV/c^2 are shown in Fig. 11. The allowed region is above the contour. It can be seen from Fig. 11 that the limits on $m(W_2)$ are essentially the same for $m(\nu_{\mu R})\leq1$ MeV/c^2, but begin to drop rapidly below that value for $m(\nu_{\mu R})>6$ MeV/c^2. The valley at $m(\nu_{\mu R})=9$ MeV/c^2 corresponds to a 2.5σ deviation of $m(W_2)$ from ∞. For $m(\nu_{\mu R})\geq17$ MeV/c^2 the limits on $m(W_2)$ decrease dramatically since the end point of the $V+A$ spectrum with a massive $\nu_{\mu R}$ approaches the minimum $x=0.97$ used in the fit of the spin-held data. The small discrepancy between the limit for $m(\nu_{\mu R})=0$ in Fig. 11 and the value quoted earlier in Sec. VII B is mainly due to a different treatment of the systematic errors.

H. Conclusions

We have made a precise measurement of the end point e^+ decay rate opposite to the spin of a decaying μ^+. Our main conclusion is that the measurement is consistent with the $V-A$ model of weak interactions. We have used the result to deduce limits on the mass of the predominantly right-handed boson W_2 and the left-right mixing angle ζ in the left-right-symmetric models, the $\nu_{\mu L}$ mass and helicity in π^+ decay, non-($V-A$) couplings in helicity projection form, the mass scale of composite leptons, and the branching ratio for $\mu\rightarrow e+f$, where f (familon) is the neutral massless Nambu-Goldstone boson associated with flavor-symmetry breaking.

We briefly consider the reduction in the error on $\xi P_\mu\delta/\rho$ that would be necessary to improve the limit on $m(W_2)$ by a factor of ~2. Assuming a central value of $\xi P_\mu\delta/\rho=1$, the 90% confidence limit $m(W_2)>800$ GeV/c^2 (with the left-right mixing angle ζ unconstrained) would require a combined statistical and systematic error of $\pm1.1\times10^{-4}$. In view of several sources of possible systematic error exceeding 10^{-4}, which are discussed in Sec. VI and Appendix C, such accuracy would be very difficult to achieve with our experimental method.

In the absence of novel experimental techniques, the discovery of W_2, assuming that its mass is in the TeV region, will have to await the advent of high-energy supercolliders. Eichten *et al.*[38] have considered the production of a possible W_2 or an associated neutral Z_2 at pp or $p\bar{p}$ machines. As a discovery criterion they adopted the requirement that 1000 gauge bosons are produced in the rapidity interval $|y|<1.5$. For a $p\bar{p}$ collider with a center-of-mass energy of 40 TeV, for example, maximum W_2 masses of 2.4, 4.7, and 8.0 TeV/c^2 were obtained for integrated luminosities of 10^{38}, 10^{39}, and 10^{40} cm^{-2}. For the same luminosities the maximum Z_2 masses were 1.9, 3.8, and 7.1 TeV/c^2. For the present moment, however, no W_2 or Z_2 signature is found; our data and those of many other experiments remain consistent with the standard $SU(2)_L\times U(1)$ electroweak model.

ACKNOWLEDGMENTS

We are indebted to the entire TRIUMF management and staff for their strong support of this experiment. In its early stages we benefited from discussions with J. Brewer, R. Cahn, K. Crowe, K. Halbach, and W. Wenzel, and from the technical contributions of C. Covey, R. Fuzesy, F. Goozen, P. Harding, M. Morrison, and P. Robrish. This research was supported in part by the U.S. Department of Energy through Contracts Nos. DE-AC03-76SF00098 and AC02-ER02289. The research described in this paper was performed in partial fulfillment of the requirements for the Ph.D. degree at the University of California, Berkeley.

APPENDIX A: STOPPING TARGETS

The muons were stopped in high-purity ($\geq99.99\%$) metal foils or in liquid He. Since foils of optimum thick-

TABLE V. Composition and thickness of the muon-stopping targets.

Target	Run	Thickness (mg/cm^2)	Residual thickness (mg/cm^2)	Residual straggling lengths
Ag	1	273	96	8.1
Al	1,2,3	150	35	4.6
Al (thick)	2	285	171	22.6
Au	1,2	6×6.6 Al	53 Au	4.1
		193 Au	6.6 Al	
		6.6 Al	Total 60	
		Total 239		
Cu	2	6×6.6 Al	16 Cu	2.5
		110 Cu	6.6 Al	
		6.6 Al	Total 23	
		Total 156		
Cu (thick)	1,2	222	81	8.3
He	1	38 Al	86 He	17.2
		150 He	38 Al	
		38 Al	Total 124	
		Total 226		

ness were unavailable, the stopping targets were made either of two back-to-back foils, or of a single foil preceded and followed by 0.001-in. aluminum foils.

The stopping target thicknesses are tabulated in Table V. The compositions of targets having 0.001-in. Al foils are listed in upstream to downstream order. The mean amount of target material encountered by decay positrons is listed as "residual thickness." The residual thickness is also tabulated in terms of calculated μ^+ rms range straggling lengths. The effect of the 1% $\Delta p/p$ momentum bite has been included. Comparison of the calculated ranges with an experimental range curve taken in run 2 (i.e., the second data-taking run) indicates that the error on the number of the residual straggling lengths is unlikely to exceed ± 0.5.

The Ag and He targets were used only in run 1. The residual thicknesses and straggling lengths for the other targets apply only to run 2. For runs 1 and 3 the residual thicknesses for Al, Au, and Cu varied by small amounts from the run 2 values due to the use of magic gas (30% isobutane, 69.7% argon, 0.3% freon) in proportional chambers for run 2 and the presence of an additional proportional chamber upstream of the target in run 3. We mention here another minor difference between runs 1, 2, and 3. During run 1 the solenoid bore was filled with methane-8% methylal gas; during run 2, a He bag was placed in the region between the drift chambers D2 and D3 (see Fig. 3); and during run 3 the He bag was removed and the solenoid bore was exposed to air.

APPENDIX B: COMPUTATION OF $\cos(\theta_{av})$

Here we address the question of what value should be assigned to $\cos\theta_{av}$ in Eq. (5.1). This topic is considered in detail because the data were fitted in subsets in which the variation in $\cos\theta$ was much greater than the error on the end-point rate $r(\theta_{av})$ and because any error in $\cos\theta_{av}$ propagated into the same error in $\xi P_\mu \delta/\rho$.

Recall that in the expression for the muon-decay spectrum $\cos\theta$ was defined as $-\hat{s}_\mu \cdot \hat{p}_e$, where $\hat{s}_\mu$ and $\hat{p}_e$ are the unit vectors corresponding to the directions of muon spin and positron momentum at the μ^+ decay vertex. At the π^+ decay vertex the muon spin is parallel or antiparallel to the muon momentum (massless neutrinos have been assumed; μ^+ helicity is always -1 for $V-A$). For the moment let us ignore the effects of scattering, finite chamber resolution, and finite accuracy of track extrapolation. The corrections to $\cos\theta_{av}$ due to these factors will be considered in Appendixes C, D, and E. We can therefore assume that the spin direction of a muon when it enters a stopping target is given by the extrapolation of the measured muon track, and similarly that the direction of the positron momentum at the decay vertex is given by the extrapolation of the measured positron track.

Let θ_μ, ψ_μ and θ_e, ψ_e be the polar and azimuthal angles with respect to the longitudinal field axis for $-\hat{s}_\mu$ (the minus sign is for convenience) and $\hat{p}_e$, respectively. Since muon spins precessed very rapidly in the strong longitudinal field, ψ_μ would have been difficult to measure. However, it was not necessary to measure ψ_μ, for it will be shown that it is sufficient to know just θ_μ.

To distinguish the spin direction $\hat{s}_\mu$ at the μ^+ decay vertex from the spin direction when a muon enters the stopping target, we denote the former by $\hat{s}_{\mu,v}$ and the latter by $\hat{s}_{\mu,\text{ent}}$. We will ignore muon scattering in the stopping target, so that $\theta_{\mu,v}$ is identical to $\theta_{\mu,\text{ent}}$, and both will be denoted by θ_μ.

Our goal is to derive the expressions (B3) and (B5) which define $\cos\theta_{av}$. First, we will have to compute the positron spectrum for the spin-held data in terms of the theoretical decay rate, the angular and momentum acceptance functions, and the angular distribution of the incoming muons. The angular distribution we need is that of muon spins (i.e., the $\hat{s}_{\mu,v}$ distribution) for muons reaching a stopping target. We will now show that this distribution is independent of the azimuthal angle $\psi_{\mu,v}$. It is important to distinguish the $\hat{s}_{\mu,v}$ distribution for the

muons reaching a stopping target from the $\hat{\mathbf{s}}_{\mu,v}$ distribution for events in the spin-held data. Although the former distribution is independent of $\psi_{\mu,v}$, the latter distribution does in fact depend on $\psi_{\mu,v}$ if the angular acceptance for positrons is ψ_e dependent. It is the former distribution which will be needed in the computation of the positron spectrum for the spin-held data.

Let $Q(\theta_\mu,\psi_{\mu,\text{ent}})$ describe the angular distribution of $\hat{\mathbf{s}}_{\mu,\text{ent}}$ for muons reaching a stopping target, after all software cuts relevant to muons have been applied. Muon spins precess about the longitudinal field axis very rapidly (40 MHz for 0.3 T and 150 MHz for 1.1 T) compared to the muon lifetime $\tau_\mu=2.2$ μsec. This implies that for a muon, arriving with the spin direction given by $(\theta_\mu,\psi_{\mu,\text{ent}})$, the probability of the muon-spin direction at the decay vertex being $(\theta_\mu,\psi_{\mu,v})$ is independent of $\psi_{\mu,v}$. Since the $\hat{\mathbf{s}}_{\mu,v}$ angular distribution, for the muons reaching a stopping target, is independent of $\psi_{\mu,v}$, it can be written as

$$R(\theta_\mu)=(1/2\pi)\int_0^{2\pi} Q(\theta_\mu,\psi_{\mu,\text{ent}})d\psi_{\mu,\text{ent}} .$$

The muon-decay spectrum may be written as

$$S(x,\cos\theta)=a(x)+b(x)\cos\theta .$$

For the spin-held data in one of the $\cos\theta_e$ bins, let $A(\theta_e,\psi_e,x)$ denote the total acceptance function for positrons, including the selection process bias (i.e., $\cos\theta_e$ must be in a certain range), the acceptance of the apparatus and software cuts. Ignoring statistical fluctuations, the positron spectrum $W(x)$ for the fitted subset of the spin-held data is given by

$$W(x)\sim\int[a(x)+b(x)\cos\theta]A(\theta_e,\psi_e,x)R(\theta_\mu)d\omega_e d\omega_\mu , \tag{B1}$$

where $d\omega$ denotes the integration over the angular phase space, i.e., $d\omega_e=d(\cos\theta_e)d\psi_e$, and

$$\cos\theta=\cos\theta_\mu\cos\theta_e+\sin\theta_\mu\sin\theta_e\cos\psi_\mu\cos\psi_e +\sin\theta_\mu\sin\theta_e\sin\psi_\mu\sin\psi_e .$$

From now on ψ_μ always denotes $\psi_{\mu,v}$.

We make the assumption that the x acceptance is independent of $\cos\theta_e$. In practice this was not true, and we will return to this issue shortly. Under this assumption, $A(\theta_e,\psi_e,x)$ can be written as a product of two acceptance functions

$$A(\theta_e,\psi_e,x)=A(\theta_e,\psi_e)A(x) .$$

If the spectrum $W(x)$ is not fitted according to (5.5), $\cos\theta_{\text{av}}$ is defined by

$$N[a(x)+b(x)\cos\theta_{\text{av}}]A(x) =\int[a(x)+b(x)\cos\theta]A(\theta_e,\psi_e)A(x)R(\theta_\mu)d\omega_e d\omega_\mu , \tag{B2}$$

where N is the normalization. Hence

$$\cos\theta_{\text{av}}=\frac{\int A(\theta_e,\psi_e)R(\theta_\mu)\cos\theta d\omega_e d\omega_\mu}{\int A(\theta_e,\psi_e)R(\theta_\mu)d\omega_e d\omega_\mu} . \tag{B3}$$

Note that $\cos\theta_{\text{av}}$ is *not* $\cos\theta$ averaged over the data, which is given by

$$\langle\cos\theta\rangle=\frac{\int\cos\theta[a(x)+b(x)\cos\theta]A(\theta_e,\psi_e)A(x)R(\theta_\mu)d\omega_e d\omega_\mu dx}{\int[a(x)+b(x)\cos\theta]A(\theta_e,\psi_e)A(x)R(\theta_\mu)d\omega_e d\omega_\mu dx} . \tag{B4}$$

Since $R(\theta_\mu)$ is independent of ψ_μ, the ψ_μ-dependent terms in $\cos\theta$ vanish in (B3) after integration over ψ_μ, and hence in (B3) $\cos\theta$ can be replaced by $\cos\theta_\mu\cos\theta_e$:

$$\cos\theta_{\text{av}}=\frac{\int\cos\theta_\mu\cos\theta_e A(\theta_e,\psi_e)R(\theta_\mu)d\omega_e d\omega_\mu}{\int A(\theta_e,\psi_e)R(\theta_\mu)d\omega_e d\omega_\mu} . \tag{B5}$$

One may think of $\cos\theta_\mu\cos\theta_e$ as $\cos\theta$ averaged over one spin-precession period ($T\ll\tau_\mu$):

$$\cos\theta_\mu\cos\theta_e=-(1/T)\int_0^T\hat{\mathbf{s}}_\mu(t)\cdot\hat{\mathbf{p}}_e dt . \tag{5.2}$$

The expression (B5) is our desired result. However, it was not possible to compute $\cos\theta_{\text{av}}$ according to (B5) since $A(\theta_e,\psi_e)$ and $R(\theta_\mu)$ were not known *a priori*. Instead, $\cos\theta_{\text{av}}$ was computed from $\cos\theta_\mu\cos\theta_e$ averaged over the spin-held data

$$\langle\cos\theta_\mu\cos\theta_e\rangle=\frac{\int\cos\theta_\mu\cos\theta_e[a(x)+b(x)\cos\theta]A(\theta_e,\psi_e)A(x)R(\theta_\mu)d\omega_e d\omega_\mu dx}{\int[a(x)+b(x)\cos\theta]A(\theta_e,\psi_e)A(x)R(\theta_\mu)d\omega_e d\omega_\mu dx} , \tag{B6}$$

to which two small corrections had to be added. The first correction compensated for the difference between $\langle\cos\theta_e\cos\theta_\mu\rangle$, given by (B6), and the acceptance-weighted average $\cos\theta_e\cos\theta_\mu$, defined by (B5). This correction was target independent. The second correction was due to the difference between $\langle\cos\theta_\mu\cos\theta_e\rangle$ computed from the measured tracks, and $\langle\cos\theta_\mu\cos\theta_e\rangle$ if it were computed from the true values of θ_μ and θ_e. This difference was mostly due to scattering, although finite chamber resolution also contributed. Since positron scattering depended on the target, the second correction was target dependent. The computation of these corrections is described in Appendixes C and D.

We now return to the issue of $\cos\theta_e$-dependent x accep-

tance. If x acceptance depends on $\cos\theta_e$, $\cos\theta_{\rm av}$ is not rigorously defined, since the equality (B2) can no longer be written. However, if the spectrum $W(x)$ is fitted as in (5.5), with $\cos\theta_{\rm av}$ computed from $\langle\cos\theta_\mu\cos\theta_e\rangle$ and the corrections mentioned above, then the systematic error in $r(\theta_{\rm av})$ will be negligibly small provided that the variation in x acceptance is small for the range of $\cos\theta_e$ in the data. Therefore, in order to minimize the systematic error in $r(\theta_{\rm av})$ due to $\cos\theta_e$-dependent x acceptance, the data were fitted in five $\cos\theta_e$ bins 0.005 wide, $0.975\le\cos\theta_e\le 1$. Events with $\cos\theta_e\le 0.975$ were dropped from analysis since they had low statistical power. If the five $\cos\theta_e$ bins were fitted together, the systematic error in $r(\theta_{\rm av})$ due to $\cos\theta_e$-dependent acceptance would have been $\pm 1\times 10^{-4}$. When each $\cos\theta_e$ bin was fitted separately, the systematic error in $r(\theta_{\rm av})$ was smaller than 0.2×10^{-4} for each $\cos\theta_e$ bin. It was checked that the result from fitting the five $\cos\theta_e$ bins separately was consistent with the result obtained when all $\cos\theta_e$ bins were fitted together.

APPENDIX C: CORRECTION DUE TO MULTIPLE SCATTERING AND FINITE CHAMBER RESOLUTION

Here we describe the computation of the correction to $\cos\theta_{\rm av}$ due to scattering and finite chamber resolution. We denote $\langle\cos\theta_\mu\cos\theta_e\rangle$ computed from the measured tracks by $\langle\cos\theta_{\rm meas}\rangle$, and $\langle\cos\theta_\mu\cos\theta_e\rangle$ if it were computed from the true values of θ_μ and θ_e by $\langle\cos\theta_{\rm true}\rangle$. The unit vector given by the extrapolation of the measured muon track to the stopping target will be denoted by $\hat{\mathbf{p}}_{\mu,\rm meas}$, and $\theta_{\mu,\rm meas}$ will denote the corresponding polar angle with respect to the solenoid axis. $\theta_{\mu,\rm true}$ will denote the true polar angle of $-\hat{\mathbf{s}}_\mu$ at the decay vertex.

Muon depolarization due to scattering with unpolarized electrons, which is considered in Appendix E, will be ignored. Coulomb scattering is relativistically helicity conserving and nonrelativistically spin conserving. The nonrelativistic limit applies to the μ^+, which initially have $\beta=0.27$ (when a muon with helicity ± 1 scatters by an angle θ, muon polarization with respect to the initial direction changes by $\approx\theta^2\beta^4/8$). It can therefore be assumed that the spin polar angle θ_μ, when a muon enters the stopping target, is identical to $\theta_{\mu,\rm true}$. The true direction of muon spin when the muon enters the stopping target will be denoted by $\hat{\mathbf{s}}_{\mu,\rm ent}$. Similarly, let $\hat{\mathbf{p}}_{e,\rm true}$ denote the direction of e^+ momentum at the decay vertex, and $\theta_{e,\rm true}$ be the corresponding polar angle. The unit vector given by the extrapolation of the measured positron track to the stopping target will be denoted by $\hat{\mathbf{p}}_{e,\rm meas}$, and $\theta_{e,\rm meas}$ will denote the corresponding polar angle.

We seek the correction $\langle\cos\theta_{\rm true}\rangle-\langle\cos\theta_{\rm meas}\rangle$. Since $\cos\theta_\mu$ and $\cos\theta_e$ are both very close to 1,

$$\cos\theta_\mu\cos\theta_e\approx\cos\theta_\mu+\cos\theta_e-1\ ,$$

and hence

$$\langle\cos\theta_{\rm true}\rangle-\langle\cos\theta_{\rm meas}\rangle\approx(\langle\cos\theta_{\mu,\rm true}\rangle-\langle\cos\theta_{\mu,\rm meas}\rangle)+(\langle\cos\theta_{e,\rm true}\rangle-\langle\cos\theta_{e,\rm meas}\rangle)\ . \tag{C1}$$

We consider qualitatively various contributions to the muon average in (C1), i.e., to the first term on the right-hand side. Similar arguments will apply for positrons. There are several sources of misalignment between $\hat{\mathbf{s}}_{\mu,\rm ent}$ and $\hat{\mathbf{p}}_{\mu,\rm meas}$. Before the muon enters the vacuum window separating the beamline from the muon polarimeter (it is located just in front of the proportional chamber P1; see Fig. 3), $\hat{\mathbf{s}}_\mu$ and $\hat{\mathbf{p}}_\mu$ are misaligned due to scattering in the production target. Muon scattering in the material (~ 50 mg/cm^2) upstream of the stopping target contributes further to the misalignment. Although scattering of the muons is assumed to be spin conserving, the muon-spin direction does change between the vacuum window and the stopping target due to spin precession in the longitudinal field.

In order to estimate the effects of muon scattering in the production target and in the material upstream of the stopping target, let us ignore the magnetic field in the stopping target region. It can therefore be assumed that muon-spin direction does not change when a muon travels from the vacuum window to the stopping target. Let us denote the true direction of the muon momentum before the muon enters the P1 vacuum window by $\hat{\mathbf{p}}_i$ (subscript i stands for "initial"). Let θ_i be the corresponding polar angle. The muon average in (C1) can be rewritten as

$$(\langle\cos\theta_{\mu,\rm true}\rangle-\langle\cos\theta_i\rangle)+(\langle\cos\theta_i\rangle-\langle\cos\theta_{\mu,\rm meas}\rangle)\ . \tag{C2}$$

Without loss of generality, we may assume that at the π^+ decay vertex $\hat{\mathbf{s}}_\mu$ is always antiparallel to $\hat{\mathbf{p}}_\mu$. Let us consider the first term in (C2). The misalignment between $\hat{\mathbf{s}}_{\mu,\rm ent}$ (which determines $\cos\theta_{\mu,\rm true}$ since the magnetic field is ignored) and $\hat{\mathbf{p}}_i$ is due to scattering in the production target. For simplicity, let the scattering angle ϕ_1 in the production target be the same for all muons. The angle ϕ_1 between $\hat{\mathbf{s}}_\mu$ and $\hat{\mathbf{p}}_\mu$ is preserved by the magnetic field in the beamline, where muons are transported in vacuum. At the vacuum window $\hat{\mathbf{s}}_\mu$ is randomly misaligned with respect to $\hat{\mathbf{p}}_i$ by an angle ϕ_1. By a simple computation

$$\langle\cos\theta_{\mu,\rm true}\rangle=\langle\cos\theta_i\rangle\cos\phi_1 \tag{C3}$$

and since ϕ_1 is small (~ 30 mrad) and $\cos\theta_i\approx 1$,

$$(\langle\cos\theta_{\mu,\rm true}\rangle-\langle\cos\theta_i\rangle)\approx-\phi_1{}^2/2\ . \tag{C4}$$

We now consider the second term in (C2). The misalignment between $\hat{\mathbf{p}}_i$ and $\hat{\mathbf{p}}_{\mu,\rm meas}$ is mostly due to scattering between the vacuum window and the proportional chamber P2, although finite chamber resolution and finite accuracy of track extrapolation also contribute. To a good approximation, only material upstream of the midpoint between P1 and P2 contributes to the misalignment (5×10^{-4} radiation lengths). The acceptance effects and software cuts preferentially reject events with the largest μ^+ scattering angles between the vacuum window and P2, which leads to a decrease ($\sim 6\times 10^{-4}$) in the correction. We will return to these effects below, when we consider the systematic errors in the correction, but for the moment suppose that these effects can be ignored. Again, let the angle ϕ_2 between $\hat{\mathbf{p}}_i$ and $\hat{\mathbf{p}}_{\mu,\rm meas}$ be the same for all muons. The unit vectors $\hat{\mathbf{p}}_{\mu,\rm meas}$ are randomly

misaligned with respect to p_i by an angle ϕ_2. Hence

$$\langle \cos\theta_{\mu,\text{meas}} \rangle = \langle \cos\theta_i \rangle \cos\phi_2$$

by the same computation as in (C3), and

$$(\langle \cos\theta_i \rangle - \langle \cos\theta_{\mu,\text{meas}} \rangle) \approx \phi_2^2/2 \ . \tag{C5}$$

Therefore the correction for μ^+ scattering in the material near the stopping target, given by (C5), has an opposite sign from the correction for μ^+ scattering in the production target, given by (C4).

Since the correction (C1) depends on the geometrical acceptance of the apparatus, on cuts in analysis, on angular distribution of the incoming muons, etc., it is not possible to compute it precisely by an analytical computation. Furthermore, the positron average in (C1) depends on the target so that the correction is also target dependent. The corrections were therefore computed, to a statistical error of less than $\pm 0.5\times 10^{-4}$ for each stopping target, in a full Monte Carlo simulation of the polarimeter described in Sec. V. The scattering model used in the simulation is based on the theory of Nigam, Sundaresan, and Wu.[39] The data generated in the simulation were processed through the same event reconstruction and selection algorithm as the experimental data, and the correction (C1) was computed from Monte Carlo events which passed all cuts. The correction varied by less than 2.5×10^{-4} from $\cos\theta_e = 0.975$ to $\cos\theta_e = 1$ for all targets. Hence, the correction was assumed to be the same for all $\cos\theta_e$ bins, since it was found that the error in $\xi P_\mu \delta/\rho$ due to this assumption was less than $\pm 0.5\times 10^{-4}$. The correction varied from the minimum of -7×10^{-4} to the maximum of $+2\times 10^{-4}$; the average over all targets was -1×10^{-4}. These numbers include an upward adjustment of 2×10^{-4} discussed below.

We now consider the possible systematic errors in the correction (C1). The accuracy of the scattering model, assumed to be $\pm 10\%$ in the scattering angle magnitude, leads to an error of $<1\times 10^{-4}$, but conservatively it is taken to be $\pm 1\times 10^{-4}$. As can be seen from Eqs. (C4) and (C5), the value of the correction should vary quadratically with the scattering angle magnitude if acceptance effects can be ignored. This quadratic dependence approximately holds in practice. The error due to the uncertainty in the scattering angle magnitude is relatively small because the correction for muon scattering in the production target has an opposite sign from the correction due to scattering near the stopping target: the muon part of the correction (C1) is 0.1×10^{-4} (total), compared to the contribution of scattering in the production target of -4×10^{-4}. The positron part of the correction, averaged over the stopping targets, is -1×10^{-4}.

The correction (C1) depends on the fraction of events with large scattering angles remaining in the final sample. The number of such events in the final sample is reduced because of software cuts requiring $\cos\theta_\mu \geq 0.99$ and a radius at the stopping target ≤ 1.8 cm. Also, such events have a larger beam spot at the stopping target, and consequently there is a smaller probability for a positron to be accepted by the apparatus. The correction (C1) therefore depends on the distribution of incoming μ^+ angles, and to a smaller extent on the beam spot at the target.

The true muon distribution in angles and position at the P1 vacuum window is not known since the measured distribution includes the effects of scattering. The measured distribution was obtained as follows. In the experiment, when the data was collected in the spin-precessing mode (i.e., with 70- or 110-G vertical field), approximately every thirtieth event was taken with a "μ-stop" trigger, requiring only a signature of a particle stopping in the target. The angular distribution of the measured muon tracks in such events was used in the Monte Carlo simulation.

Since essentially all muons at the P1 vacuum window are accepted by the apparatus, it is possible to estimate the true μ^+ distribution that would yield the measured distribution. When the estimated true μ^+ distribution was used to compute the correction, the muon part of the correction was $\approx 2\times 10^{-4}$ greater than it was with the measured distribution. Therefore, all corrections computed with the measured distribution were adjusted upwards by 2×10^{-4}, and a possible systematic error of $\pm 2\times 10^{-4}$ was assigned to the correction (C1) due to the uncertainty in the incoming μ^+ distribution.

Finally, the correction (C1) depends on the amount of scattering in the production target. The mean thickness of material in the production target traversed by muons is determined by the mean beam momentum, estimated to be 29.45 MeV/c. The μ^+ momentum from π^+ decay at rest is 29.79 MeV/c, which implies that the mean energy loss in the graphite production target was 0.0092 MeV, corresponding to a mean thickness traversed by muons of 6.6 mg/cm^2. An uncertainty in the mean μ^+ beam momentum of ± 0.2 MeV/c implies an uncertainty of 3.8 mg/cm^2 in the mean thickness traversed by muons, which leads to a possible systematic error in the correction of $\pm 2\times 10^{-4}$.

When these three systematic errors are added in quadrature, the combined possible systematic error in the correction (C1) becomes $\pm 3\times 10^{-4}$. The correction averaged over all targets was -1×10^{-4}.

APPENDIX D: CORRECTION DUE TO USE OF DATA-AVERAGED $\cos\theta_\mu \cos\theta_e$

We seek a correction to $\cos\theta_{\text{av}}$ due to the difference between the expression (B5) defining $\cos\theta_{\text{av}}$ and the data averaged $\cos\theta_\mu \cos\theta_e$ given by (B6). The correction required is given by

$$\cos\theta_{\text{av}} - \langle \cos\theta_\mu \cos\theta_e \rangle \ . \tag{D1}$$

Here it is assumed that $\langle \cos\theta_\mu \cos\theta_e \rangle$ has been computed from the true values of θ_μ and θ_e.

It was shown in Appendix B that when statistical fluctuations are ignored, the positron spectrum for the fitted subset of the spin-held data is given by

$$W(x) \sim \int [a(x) + b(x)\xi P_\mu \cos\theta] A(\theta_e, \psi_e) \times A(x) R(\theta_\mu) d\omega_e d\omega_\mu \ , \tag{D2}$$

where $a(x)$ and $b(x)$ are the angle-dependent and angle-independent parts of the muon-decay rate; $A(\theta_e, \psi_e)$ is the angular acceptance function for positrons, assumed to be independent of the x acceptance function $A(x)$; $R(\theta_\mu)$

denotes the θ_μ distribution of muon spins at the decay vertex for muons reaching the stopping target (the distribution is isotropic in ψ_μ); $d\omega$ denotes the integration over the angular phase space, i.e., $d\omega_e = d(\cos\theta_e)d\psi_e$, and

$$\cos\theta = \cos\theta_\mu\cos\theta_e + \sin\theta_\mu\sin\theta_e\cos\psi_\mu\cos\psi_e + \sin\theta_\mu\sin\theta_e\sin\psi_\mu\sin\psi_e \ .$$

The two terms in the expression for $\cos\theta$ which contain ψ_μ, vanish in (D2) after integration. Aside from $\cos\theta$, only $A(\theta_e,\psi_e)$ in (D2) depends on ψ_e. Hence, $W(x)$ can be rewritten in terms of the angular acceptance function which depends only on θ_e:

$$A(\theta_e) = \int A(\theta_e,\psi_e)d\psi_e \ . \tag{D3}$$

This fact will be useful for the discussion below.

The correction (D1) depends on the range of $\cos\theta_e$ in the fitted data set, and also on the minimum x in the fit of the spin-held data. For $\cos\theta_e$ bins 0.005 wide and $x_{\min}=0.97$, the correction was small, only $+1\times10^{-4}$, and to an accuracy of $\pm0.1\times10^{-4}$ it was the same for all $\cos\theta_e$ bins. The correction was computed by evaluating the spectrum $W(x)$ numerically, using the estimated true $R(\theta_\mu)$ distribution (see Appendix C), and assuming that $A(x)$ and $A(\theta_e,\psi_e)$ were constant.

It was checked that the correction changed negligibly for realistic $A(x)$ and $A(\theta_e)$. The x acceptance varied the most in the smallest $\cos\theta_e$ bin (i.e., $0.975 \le \cos\theta_e < 0.98$ bin). When the spin-precessed data were combined from all targets and fitted according to (5.3), with $A(x)$ given by (5.4), it was found that the x acceptance in this $\cos\theta_e$ bin fell by 17% at $x=0.93$ and by 1.5% at $x=1$, relative to the acceptance maximum at $x=0.985$. The correction (D1) changed by less than 0.1×10^{-4} when this $A(x)$ was used in the computation of $W(x)$.

The angular acceptance $A(\theta_e)$ for the spin-held data should be similar to $A(\theta_e)$ for the spin-precessed data. The latter is given by the number of events as a function of $\cos\theta_e$, since after timing cuts the spin-precessed data is equivalent to the unpolarized, i.e., $P_\mu=0$, data, and the angular distribution of decay positrons for $P_\mu=0$ data is isotropic. The angular acceptance at $\cos\theta_e=0.975$ fell by $\sim20\%$ relative to $\cos\theta_e=1$. The correction (D1) changed by less than 0.1×10^{-4} for a 10% variation in $A(\theta_e)$ in a single $\cos\theta_e$ bin.

Since $A(\theta_e)$ depends on x, one may define $\cos\theta_{\rm av}$ using the angular acceptance function for the center of the fitted $\cos\theta_e$ bin. If such acceptance function is denoted by $A_c(\theta_e)$, then

$$\cos\theta_{\rm av} = \frac{\int \cos\theta_\mu\cos\theta_e A_c(\theta_e)R(\theta_\mu)d(\cos\theta_e)d\omega_\mu}{\int A_c(\theta_e)R(\theta_\mu)d(\cos\theta_e)d\omega_\mu} \ .$$

With this definition of $\cos\theta_{\rm av}$ the correction (D1) is still accurate to $\pm0.1\times10^{-4}$ for a realistic variation of $A(\theta_e)$ with x.

APPENDIX E: CORRECTION DUE TO MUON DEPOLARIZATION IN SCATTERING WITH UNPOLARIZED ELECTRONS

Here we describe the computation of the correction to $\xi P_\mu\delta/\rho$ due to muon depolarization in scattering with unpolarized electrons during the stopping process. We denote by the unit vector $\hat{\sigma}_\mu$ the direction the muon spin would have if scattering with electrons were absent. Muon polarization with respect to $\hat{\sigma}_\mu$ is reduced due to spin-exchange effects in scattering with unpolarized electrons. The polarization with respect to $\hat{\sigma}_\mu$ would have been preserved in the absence of scattering. For simplicity, let us assume that at the π^+-decay vertex the muon spin is antiparallel to $\hat{\mathbf{p}}_\mu$, as it is for a pure $V-A$ interaction. Let the solenoid axis define the z direction. Muon depolarization with respect to $\hat{\sigma}_\mu$ in scattering with unpolarized electrons during the stopping process will be denoted by ΔP. We will continue to assume that Coulomb scattering from nuclei is spin conserving, just as we have done in Appendix B. The expectation value of the muon spin $\hat{\mathbf{s}}_\mu$ with respect to $\hat{\sigma}_\mu$ is

$$\langle\hat{\mathbf{s}}_\mu\rangle_{\hat{\sigma}_\mu} = (\hbar/2)(1-\Delta P) \ ,$$

which implies that the expectation value with respect to the z axis is

$$\langle\hat{\mathbf{s}}_\mu\rangle_z = (1-\Delta P)\langle\hat{\sigma}_\mu\rangle_z \ .$$

In Appendix C the correction (C1), due to the difference between $\langle\cos\theta_\mu\cos\theta_e\rangle$ computed from the measured tracks and $\langle\cos\theta_\mu\cos\theta_e\rangle$ computed from the true values of θ_μ and θ_e, has been found assuming that $\cos\theta_{\mu,\rm true}$ is given by the z component of $\hat{\sigma}_\mu$, rather than by $\langle\hat{\mathbf{s}}_\mu\rangle_z$. Hence, after the correction (C1) has been added to $\langle\cos\theta_\mu\cos\theta_e\rangle$, the resulting value must in addition be multiplied by $(1-\Delta P)$. Since ΔP is only 7×10^{-4}, as will be shown below, and $\langle\cos\theta_\mu\cos\theta_e\rangle$ is >0.97, an upward correction equal to ΔP has been made directly to the result for $\xi P_\mu\delta/\rho$.

We now consider the computation of ΔP. It was shown by Ford and Mullin[28] that for a nonrelativistic μ^+ which scatters with unpolarized e^- through a center-of-mass angle θ, the probability that the final μ^+ spin direction is parallel ($\epsilon=1$) or antiparallel ($\epsilon=-1$) to the initial spin is

$$Q(\epsilon,\theta) = \frac{1+\epsilon}{2} - \epsilon\frac{m^2}{\mu^2}\beta^4[\sin^2(\theta/2) - \sin^4(\theta/2) + \sin^6(\theta/2)] \ ,$$

where β is the muon velocity in the laboratory frame and $m=m_e$ and $\mu=m_\mu$. If the muons have initial polarization $P_{\mu,i}$, the polarization $P_{\mu,f}$ after one additional scatter is

$$P_{\mu,f} = P_{\mu,i}\left[1 - 2\frac{m^2}{\mu^2}\beta^4[\sin^2(\theta/2) - \sin^4(\theta/2) + \sin^6(\theta/2)]\right] .$$

The corresponding fractional energy loss is

$$w=\frac{m}{\mu}\beta^2\sin^2(\theta/2)\ .$$

One can write a differential equation for the depolarization as a function of energy. For the energy loss $dE=wE$, where E is the muon kinetic energy $E=(\gamma-1)\mu$, the rate of depolarization is

$$\frac{dP_\mu}{dE}=P_\mu(E)\left[2\frac{m}{\mu^2}\frac{\beta^2}{(\gamma-1)}[1-\sin^2(\theta/2)+\sin^4(\theta/2)]\right]\ . \tag{E1}$$

The nonrelativistic cross section is inversely proportional to $\sin^4(\theta/2)$, and hence the $\sin(\theta/2)$ terms in (E1) can be ignored. The polarization $P_\mu(E)$ will be >0.999, and can be set equal to unity on the right-hand side. Surface muons, coming from π^+ decay at rest, initially have kinetic energy $E_0=4.1$ MeV. Since muon energy loss for $E>3$ keV is almost entirely due to scattering with electrons (see Sec. III C), ΔP is given by

$$\begin{aligned}\Delta P&=\int_{3\text{ keV}}^{E_0}2\frac{m}{\mu^2}\frac{\beta^2}{(\gamma-1)}dE\\&\approx 2\frac{m}{\mu^2}\int_0^{E_0}\left[2-3\frac{E}{\mu}\right]dE\\&\approx 4\frac{mE_0}{\mu^2}\left[1-\frac{3}{4}\frac{E_0}{\mu}\right]\approx 7.3\times10^{-4}\ .\end{aligned}$$

It should be noted that ΔP is relatively insensitive to the lower limit in the integration. The uncertainty in this correction is therefore estimated to be small compared to 1×10^{-4}.

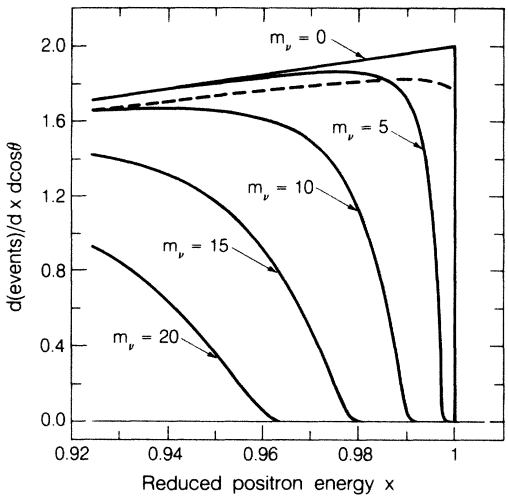

FIG. 12. The $V+A$ muon-decay rate without radiative corrections for $m(\nu_\mu)=0$, 5, 10, 15, and 20 MeV/c^2 assuming massless ν_e (solid curves), plotted vs reduced positron energy x. The dashed curve is the $V+A$ radiatively corrected decay rate for $m(\nu_\mu)=m(\nu_e)=0$. The curves are normalized so that the integral of the radiatively corrected rate is 1.

APPENDIX F: COMPUTATION OF LIMITS ON $m(W_2)$ WITH $m(\nu_{\mu R})\neq0$

We describe the analysis method used in the computation of limits on $m(W_2)$ as a function of $m(\nu_{\mu R})$ for $m(\nu_{\mu R})\leq16.5$ MeV/c^2. We assume that ν_{eR} is very light, $m(\nu_{eR})<1$ MeV/c^2, that there is no mixing between W_1 and W_2, i.e., $\zeta=0$ and $W_2=W_R$, and that there is no mixing between neutrinos.

The muon-decay rate for massive neutrinos has been calculated by Shrock.[40] If radiative corrections, positron mass, and ν_{eR} mass are neglected, the $V+A$ differential decay rate is given by

$$\frac{d^2\Gamma}{dx\,d(\cos\theta)}\sim(1-\nu^2/k^2)^2x^2\{(3-2x)+(3-x)\nu^2/k^2-\cos\theta[1-2x-(1+x)\nu^2/k^2]\}\ ,$$

where $\nu=m(\nu_{\mu R})$, $k^2=m_\mu{}^2-2m_\mu E_e$, and $x=E_e/E_0$. Here E_0 is the maximum positron energy for the spectrum with massless neutrinos (i.e., E_0 is equal to $E_{\max}$ in Sec. II). The maximum positron energy for a spectrum with a massive $m(\nu_{\mu R})$ is $E_{\max}=(m_\mu{}^2-\nu^2)/(2m_\mu)$.

Radiative corrections to the muon-decay spectrum have been calculated only for the case of massless neutrinos. Hence, in fitting with massive neutrinos we used the $V+A$ spectrum without radiative corrections, but made an adjustment (described below) to the fitted value for the $V+A$ decay rate in order to compensate for the missing corrections. The limits on $m(W_2)$ that we have computed are therefore only approximate because of the lack of radiative corrections, and also because of several simplifications in the treatment of systematic errors. The limits on $m(W_2)$ are expected to be accurate to $\sim2\%$.

The $V+A$ decay rate *without* the radiative corrections is plotted in Fig. 12 for $\cos\theta=1$ and $m(\nu_{\mu R})=0$, 5, 10, 15, and 20 MeV/c^2 (solid curves). For comparison, the radiatively corrected $V+A$ rate for $m(\nu_{\mu R})=0$ and $\cos\theta=1$ is shown by the dashed curve. The ratio of the radiatively corrected $V+A$ rate to the uncorrected rate for $m(\nu_{\mu R})=0$ is nearly independent of $\cos\theta$ for $\cos\theta$ near 1. It decreases from 0.95 at $x=0.97$ to 0.93 at $x=0.99$ approximately linearly; above $x=0.99$ it decreases much more rapidly and approaches 0 as $x\to1$.

If neutrinos are massive Majorana particles there are four distinct final states in muon decay (it is assumed that there is no neutrino mixing). If $\nu_{\mu R}$ is massive but ν_{eR} is very light, then the measured spectrum corresponding to the spin-held data will be proportional to the sum

$$S_{V-A}(x,P_\mu\cos\theta_{\rm av})+\epsilon^2S_{V+A,\nu}(x,P_\mu\cos\theta_{\rm av})\ , \tag{F1}$$

where $S_{V-A}(x,P_\mu\cos\theta_{\rm av})$ denotes the $V-A$ spectrum for muon polarization equal to P_μ and $\cos\theta=\cos\theta_{\rm av}$, ϵ is the mass-squared ratio for the gauge bosons W_1 and W_2, and $S_{V+A,\nu}(x,P_\mu\cos\theta_{\rm av})$ is the $V+A$ spectrum for a massive $\nu_{\mu R}$ with the same normalization as $S_{V-A}(x,P_\mu\cos\theta_{\rm av})$.

Recall that in the case of massless neutrinos the fitting function for the spin-held data (5.5) was based on Eq. (2.2). The sum (F1) can also be written in a form similar to Eq. (2.2):

$$[1-r(\theta_{\rm av})]S_{V-A}(x,1)+r(\theta_{\rm av})S_{V-A}(x,0)$$
$$+\epsilon^2\{[1-r(\theta_{\rm av})]S_{V+A,\nu}(x,1)+r(\theta_{\rm av})S_{V+A,\nu}(x,0)\}\ ,$$

where

$$r(\theta_{\rm av})=1-P_\mu\cos\theta_{\rm av}\ .$$

The fitting procedure for the case of massive neutrinos was therefore very similar to that for massless neutrinos described in Sec. V A and we will not describe it in detail. The primary difference was that in the fitting function for the spin-held data there was one more free parameter ϵ, which was constrained to be greater or equal to zero. For the fitting function for the spin-precessed data, it was determined that the contribution of $S_{V+A,\nu}(x,0)$ could be ignored because it changed the limit on $m(W_2)$ by less than 0.5%.

There was, however, an additional constraint on ϵ imposed by the fitted value of the relative rate at the end point $r(\theta_{\rm av})$ (i.e., of $1-P_\mu\cos\theta_{\rm av}$) since for a sufficiently light $\nu_{\mu R}$ the polarization of the muon beam delivered to the polarimeter would have been reduced by the effects of the same right-handed currents. The reduction in muon beam polarization due to possible right-handed currents is given by

$$\Delta P_\mu=2\epsilon^2\beta_\nu F(m_\nu)\ , \tag{F2}$$

where β_ν is the velocity of $\nu_{\mu R}$ in π^+ decay at rest and $F(m_\nu)$ is the fraction of muons in the beam which were produced in π^+ decays mediated by W_2. The fitted value of $r(\theta_{\rm av})$ was therefore constrained to be

$$r(\theta_{\rm av})\geq 1-(1-\Delta P_\mu)\cos\theta_{\rm av}$$

with ΔP_μ given by (F2).

The fraction $F(m_\nu)$, defined just above, decreased as $m(\nu_{\mu R})$ increased and as the momentum of the muons, produced in π^+ decays mediated by W_2, approached the lower boundary of the beamline momentum bite. For simplicity this fraction was computed assuming a uniform distribution in the 1% beam momentum bite $\Delta p/p$. The mean beam momentum was taken to be 29.45 MeV/c. $F(m_\nu)$ vanished for $m(\nu_{\mu R})>5$ MeV/c^2.

The limits on ϵ [which in turn determine the limits on $m(W_2)$] were computed for $m(\nu_{\mu R})$ varying from 0 to 16.5 MeV/c^2 in steps of 0.5 MeV/c^2. For $m(\nu_{\mu R})\geq 17$ MeV/c^2 the limits on ϵ increased dramatically since the end point of the spectrum $S_{V+A,\nu}(x,P_\mu\cos\theta_{\rm av})$ approached the minimum $x=0.97$ used in the fit of the spin-held data. In order to reduce the computational effort only one fit was made for each value of $m(\nu_{\mu R})$. The fit was made to the data from all targets in one $\cos\theta_e$ bin ($\cos\theta_e\geq 0.975$). Furthermore, since the systematic error in ϵ was different for each value of $m(\nu_{\mu R})$, only the largest systematic errors were considered. For $m(\nu_{\mu R})>5$ MeV/c^2, when there was no constraint on ϵ from $r(\theta_{\rm av})[r(\theta_{\rm av})=1-P_\mu\cos\theta_{\rm av}]$, the systematic error in $\cos\theta_{\rm av}$ did not propagate into an error in ϵ. Hence the largest systematic errors in ϵ for $m(\nu_{\mu R})>5$ MeV/c^2 were due to possible differences in $x=1$ calibration and x acceptance between the spin-held and spin-precessed data sets (see Secs. VI A and VI B). For simplicity, only these two errors were considered also for $m(\nu_{\mu R})$ less than 5 MeV/c^2.

In order to account for these systematic errors, the limits on ϵ were computed for the four different cases corresponding to $\Delta x_1=\pm 0.45\times 10^{-4}$ and $D_1=\pm 0.2$, where Δx_1 and D_1 are defined in Secs. VI A and VI B, respectively. Of the four limits the most conservative limit on ϵ was chosen corresponding to the highest value. For each fit the upper limit on ϵ was taken to be the sum of the fitted value, constrained to be greater or equal to zero, plus a positive error corresponding to an increase in χ^2 of 1.638. ($1.638=1.28^2$; the probability of an answer lying more than 1.28σ above a Gaussian with a standard deviation σ is 10%.)

As mentioned above, the limits on ϵ were computed using the spectrum $S_{V+A,\nu}(x,P_\mu\cos\theta_{\rm av})$ without radiative corrections. For $m(\nu_{\mu R})=0$ the fitted value for ϵ was compared to the value found when the radiative corrections were included. Agreement in the two values could be obtained if the former were multiplied by 1.04. Since the effect of the radiative corrections is greatest near the end point, one would expect that the adjustment in the fitted value for ϵ should be smaller for $m(\nu_{\mu R})>0$, because the spectrum for $m(\nu_{\mu R})>0$ rises more slowly near the end point (see Fig. 12). Conservatively, however, the limits on ϵ were multiplied by 1.04 for all values of $m(\nu_{\mu R})$.

The approximate limits on $m(W_2)$ vs $m(\nu_{\mu R})$, computed from the limits on ϵ assuming $m(W_1)=81$ GeV/c^2, are shown in Fig. 11 and discussed in Sec. VII G.

---

*Present address: Bell Communications Research, 331 Newman Springs Rd., Red Bank, NJ 07701-7020.

†Present address: Department of Physics, University of Colorado, Boulder, Colorado 80309.

‡Deceased.

§Present address: Department of Physics, The Johns Hopkins University, Baltimore, MD 21218.

[1]S. Glashow, Nucl. Phys. **22**, 529 (1961); S. Weinberg, Phys. Rev. Lett. **19**, 1264 (1967); A. Salam, in *Elementary Particle Theory*, edited by N. Svartholm (Almqvist & Wiksell, Stockholm, 1968).

[2]K. Mursula, M. Roos, and F. Scheck, Nucl. Phys. **B219**, 321 (1983); K. Mursula and F. Scheck, *ibid.* **B253**, 189 (1985).

[3]J. C. Pati and A. Salam, Phys. Rev. D **10**, 275 (1974); R. N. Mohapatra and J. C. Pati, *ibid.* **11**, 566 (1974); **11**, 2558 (1974); G. Senjanovic and R. N. Mohapatra, *ibid.* **12**, 1502 (1975).

[4]G. Senjanovic, Nucl. Phys. **B135**, 334 (1979).

[5]M. Gell-Mann, P. Ramond, and R. Slansky (unpublished); R. N. Mohapatra and G. Senjanovic, Phys. Rev. D **23**, 165 (1981).

[6]G. Beall, M. Bander, and A. Soni, Phys. Rev. Lett. **48**, 848 (1982); R. N. Mohapatra, G. Senjanovic, and M. D. Tran, Phys. Rev. D **28**, 546 (1983); F. J. Gilman and M. H. Reno,

Phys. Lett. **127B**, 426 (1983).
[7]J. Donahue and B. Holstein, Phys. Lett. **113B**, 382 (1982). See also I. I. Bigi and J. M. Frère, *ibid.* **110B**, 255 (1982).
[8]F. I. Olness and M. E. Ebel, Phys. Rev. D **30**, 1034 (1984).
[9]L. Wolfenstein, Phys. Rev. D **29**, 2130 (1984).
[10]M. A. B. Bég, R. V. Budny, R. Mohapatra, and A. Sirlin, Phys. Rev. Lett. **48**, 1252 (1977); B. R. Holstein and S. B. Treiman, Phys. Rev. D **16**, 2369 (1977).
[11]D. P. Stoker *et al.*, Phys. Rev. Lett. **54**, 1887 (1985).
[12]D. P. Stoker, Ph.D. thesis, Lawrence Berkeley Laboratory Report No. LBL-20324, 1985 (unpublished).
[13]The primary input to the world average is from V. V. Akhmanov *et al.*, Yad. Fiz. **6**, 316 (1967).
[14]The primary input to the world average is from J. Peoples, Nevis Cyclotron Report No. 147, 1966 (unpublished).
[15]J. Van Klinken, Nucl. Phys. **75**, 145 (1966).
[16]J. Van Klinken *et al.*, Phys. Rev. Lett. **50**, 94 (1983).
[17]D. Schrieber and F. T. Calaprice (private communication); D. Schreiber, Ph.D. thesis, Princeton University, 1983. We calculated the contour plotted in Fig. 1 using $A(0)=0.0363\pm0.0008$; ft ratio $=1.797\pm0.002$. See also F. T. Calaprice, S. J. Freedman, W. C. Mead, and H. C. Vantine, Phys. Rev. Lett. **35**, 1566 (1975).
[18]H. Abramowicz *et al.*, Z. Phys. C **12**, 225 (1982).
[19]T. D. Lee and C. N. Yang, Phys. Rev. **108**, 1611 (1957).
[20]F. Scheck, Phys. Lett. **44C**, 187 (1978).
[21]Particle Data Group, C. G. Wohl *et al.*, Rev. Mod. Phys. **56**, S1 (1984). Primary input to ρ is from Ref. 14; primary input to η is from F. Corriveau *et al.*, Phys. Lett. **129B**, 260 (1983) and S. E. Derenzo, Phys. Rev. **181**, 1854 (1969); primary input to ξP_μ is from Ref. 13; primary input to δ is D. Fryberger, Phys. Rev. **166**, 1379 (1968).
[22]Radiative corrections in muon decay are reviewed by A. M. Sachs and A. Sirlin, in *Muon Physics,* edited by V. Hughes and C. S. Wu (Academic, New York, 1975), Vol. II.
[23]M. A. B. Bég and A. Sirlin, Annu. Rev. Nucl. Sci. **24**, 579 (1974).
[24]V. Fluorescu and O. Kamei, Nuovo Cimento **61A**, 967 (1968).
[25]A. E. Pifer, T. Bowen, and K. R. Kendall, Nucl. Instrum. Methods **135**, 39 (1976).
[26]C. J. Oram, J. B. Warren, G. M. Marshall, and J. Doornbos, Nucl. Instrum. Methods **179**, 95 (1981).
[27]The deceleration and thermalization of muons in matter has been reviewed by J. H. Brewer, K. M. Crowe, F. N. Gygax, and A. Schenck, in *Muon Physics,* edited by V. Hughes and C. S. Wu (Academic, New York, 1975), Vol. III.
[28]G. W. Ford and C. J. Mullin, Phys. Rev. **108**, 477 (1957).
[29]V. Hughes, Phys. Rev. **108**, 1106 (1957).
[30]R. Sagane, W. Dudziak, and J. Vedder, Phys. Rev. **95**, 863 (1954).
[31]K. Halbach (private communication). The mathematical formalism of first-order optics approximation for cylindrically symmetric fields is outlined in Appendix A of Ref. 12.
[32]F. James and M. Roos, CERN Computer Center Reports Nos. D506 and D516 (unpublished).
[33]P. Herczeg, Phys. Rev. D (to be published).
[34]M. Abolins *et al.*, in *Proceedings of the 1982 DPF Summer Study on Elementary Particle Physics and Future Facilities, Snowmass, 1982,* edited by R. Donaldson, R. Gustafson, and F. Paige (Fermilab, Batavia, IL, 1983), p. 274; S. Yamada, in *Proceedings of the XXII International Conference on High Energy Physics, Leipzig, 1984,* edited by A. Meyer and E. Wieczorek (Akademie der Wisssenschaften der DDR, Zeuthen, East Germany, 1984), p. 72; M. Althoff *et al.*, Z. Phys. C **22**, 13 (1984).
[35]M. E. Peskin (private communication).
[36]K. D. Lane and E. Barany (private communication).
[37]F. Wilczek, Phys. Rev. Lett. **49**, 1549 (1982).
[38]E. Eichten, I. Hinchliffe, K. Lane, and C. Quigg, Rev. Mod. Phys. **56**, 579 (1984).
[39]B. P. Nigam, M. K. Sundaresan, and T. A. Wu, Phys. Rev. **115**, 491 (1959); J. B. Marion and B. A. Zimmerman, Nucl. Instrum. Methods **51**, 93 (1967).
[40]R. E. Shrock, Phys. Rev. D **24**, 1275 (1981).